Voltammetric and *In Situ* Spectroscopic Investigations on the Electrochemical Dynamics of Trioxotriangulene Neutral Radicals on Graphite Electrode Surfaces

SHOHEI KITANO

SEPTEMBER 2023

Voltammetric and *In Situ* Spectroscopic Investigations on the Electrochemical Dynamics of Trioxotriangulene Neutral Radicals on Graphite Electrode Surfaces

A dissertation submitted to

THE GRADUATE SCHOOL OF ENGINEERING SCIENCE

OSAKA UNIVERSITY

in partial fulfillment of the requirements for the degree of

DOCTOR OF PHILOSOPHY IN SCIENCE

BY

SHOHEI KITANO

SEPTEMBER 2023

Abstract

The Sustainable Development Goals provide a powerful framework for international cooperation to achieve a sustainable future for the planet including a target to address the global warming. A global energy transition away from fossil fuels to renewable energy will play an essential role to suppress carbon dioxide emissions. Due to instability risk of renewable energy, battery energy storage systems (BESSs) will be more required to manage power grid systems.

Lithium-ion batteries (LIBs) are considered to be the most suitable energy storage devices for BESSs because they are technologically mature and already widely used in various portable electronic gadgets and electric vehicles. Meanwhile, transition metal oxides currently used as cathode active materials have the risk of resource depletion, environmental pollutions, and thermal runaway. Organic cathode active materials have been explored as alternatives because of their abundant resources, environment friendliness, and high safety.

Trioxotriangulene (TOT), a stable neutral radical which possesses a spin-delocalized 25π-electronic system, is a promising material due to the large specific capacity owing to four-stage redox ability. However, capacity degradation upon charge/discharge cycles is a critical issue due to dissolution and/or deformation of TOT crystals because the solubility of TOT significantly changes depending on its valence state. The mechanism of the redox processes and structural changes of TOT in the vicinity of electrode surfaces is not fully understood so far.

In this dissertation, voltammetric and *in situ* infrared (IR) spectroelectrochemical investigations on the redox processes of TOT on graphite electrode surfaces were performed. Elucidation of electrochemical dynamics of TOT on the graphite electrode

surfaces is likely to lead better understanding of electrode design and improvement of battery performance.

Chapter 1 provides the general introduction and the purpose of this dissertation. After discussing the social positioning of this study, a brief review of organic cathode active materials including TOT and *in situ* analyses at the interface of electrolyte/active materials are presented. Chapter 2 describes the principles and experimental techniques including voltammetry, Fourier transform IR spectroscopy, and electron microscopy, which were employed in this dissertation.

To obtain the information of electrochemical behavior and structural changes of TOT on the redox process, voltammetry and electron microscopy were adopted in Chapter 3. Voltammetric measurements of the TOT monoanion solution on the graphite electrode revealed the irreversible redox process. The results suggested an orientation-dependent redox activity; reducible and dissolvable in face-on orientation, whereas not in edge-on orientation. A primitive schematic of redox mechanism was proposed from the results of voltammetry and electron microscopy.

The electrochemical dynamics of TOT on the graphite electrode surface was investigated using *in situ* IR spectroelectrochemistry in Chapter 4 to confirm the model proposed in Chapter 3. *In situ* analyses successfully characterized the alignment of the columnar crystals of the TOT neutral radicals at a different electrode potential, including the possible origins of the irreversible redox reaction of TOT on the graphite electrode. A plausible mechanistic redox model was proposed as a summary.

Chapter 5 summarizes the entire dissertation and offers perspectives on future investigations. This dissertation showed that the orientations of π-radical organic active materials on graphite surface was important for the electron transfer characteristics. The

author hope that this dissertation will lead to a better understanding of electrode design for organic rechargeable batteries.

Contents

Chapter 1
General Introduction

1-1 Background: The Sustainable Development Goals

Human civilization began with the use of energy. The discovery of fire enabled us to produce heat for local heating, lighting, cooking and material processing purposes by biomass combustion. The Industrial Revolution in the late 1700s caused a paradigm shift to the use of fossil fuels, such as coal, oil, and natural gas, as the primary sources of energy. As the population grows over the years, the demand for non-renewable resources also increases many times over because the environment is on the brink of destruction. At the same time, an economic system reliant on fossil fuels may have been causing changes to our climate. The issues on the energy problem are directly related to major challenges which the world faces today, including adaptation to climate change, food security, and transport. Therefore, it is indispensable for us to transfer to more environment-friendly and renewable sources of energy which is accessible all over the world.

The Sustainable Development Goals (SDGs), adopted by the United Nations General Assembly (UNGA) in 2015, provide a powerful framework for international cooperation to achieve a sustainable future for the planet.[1] They consist of 17 SDGs and their 169 targets, which are urgent call for action in a global partnership by all countries regardless of developed or developing. They are recognized as important strategies not only for tackling climate change and preserving our oceans and forests but also for improving health and education, reducing inequality, and spurring economic growth. The global goal on energy – SDG 7 – encompasses three key targets: ensure affordable, reliable, and universal access to modern energy services (SDG 7.1); increase substantially the share of renewable energy in the global energy mix (SDG 7.2); and double the global rate of improvement in energy efficiency (SDG 7.3).

Achieving SDG 7 is also expected to promote actions to meet the Paris Agreement on climate change and SDG 13, the goal on climate action. A transition away from fossil fuels to low-carbon solutions will play an essential role because energy-related carbon dioxide (CO_2) emissions represent two-thirds of all greenhouse gases.[2] A global energy transition has been advanced by technological innovation since Kyoto Protocol in 1997, especially in the field of renewable energy (Figure 1-1-1). Promoting renewable energy and electrification measures can potentially achieve 75% reduction of the energy-related CO_2 emissions by 2050, according to the REmap scenario (Figure 1-1-2).[3] Therefore, these measures are urgently needed to meet the objectives of limiting average global surface temperature increase below 2℃.

Despite the advantages and sustainability of renewable energy, there remain two major issues when integrating it into the power grid.[4] First, it is well-known that renewable energy production strongly depends on local weather and climate conditions. The consequent intermittent and stochastic characteristics of renewable energy can cause instability in the power systems. Second, as the penetration of renewable energy increases, it is more difficult for existing conventional power systems to accommodate the increase in renewable energy generation. Consequently, solar energy needs to be curtailed due to a limited capability to accommodate this fluctuation, thereby reducing the economic and environmental benefits of renewable energy integration.

One of the possible solutions for the above issues is to use Energy Storage Systems (ESS) to facilitate the increasing penetration of renewable energy by absorbing and releasing power in different time horizons.[5] Of the various types of ESS technology available, Battery Energy Storage Systems (BESS) have attracted considerable attention

with clear advantages like fast response, controllability, and geographical independence. High-performance energy storage devices are required to realize practical BESS.

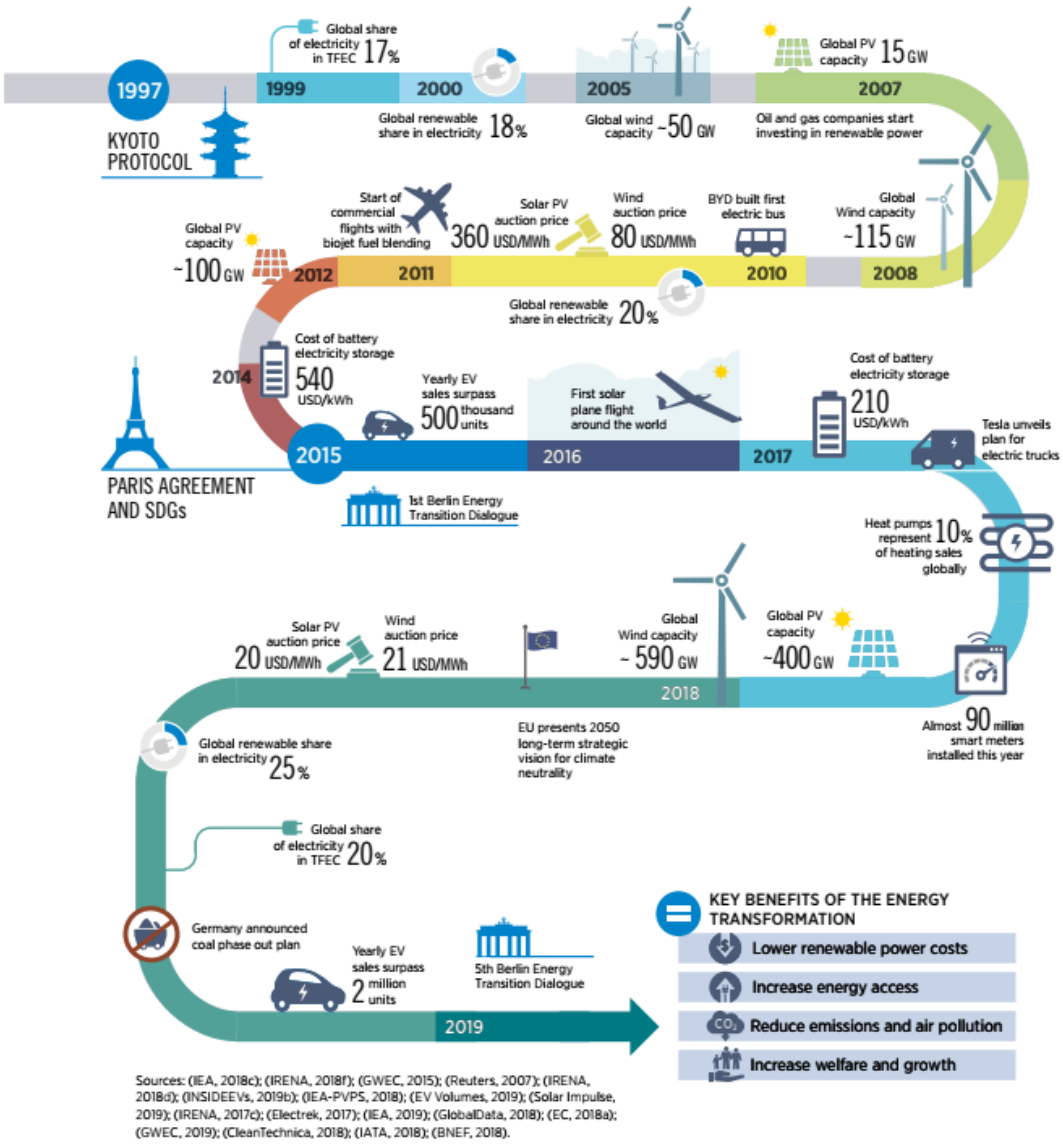

Figure 1-1-1. Recent progress of energy transformation.[3]

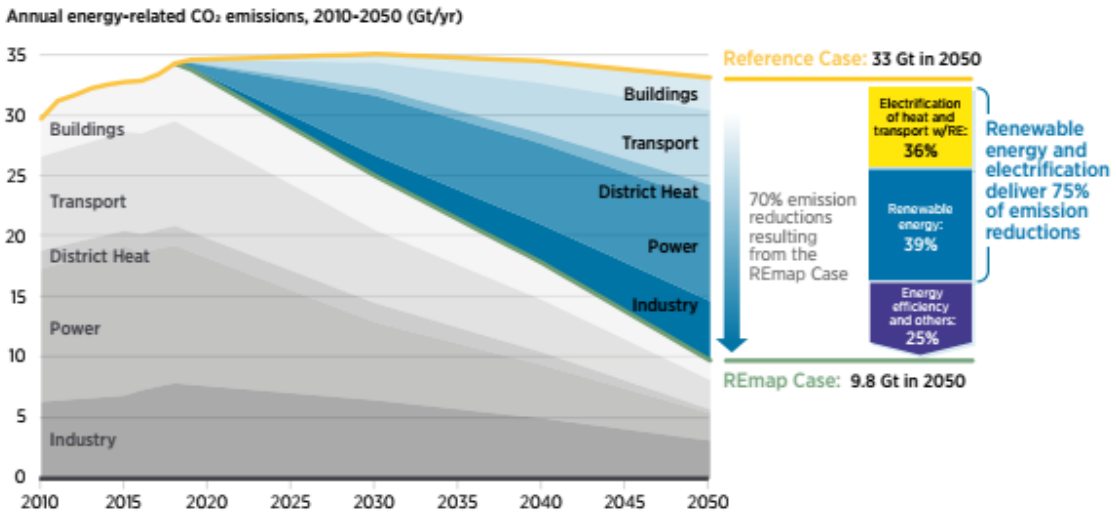

Figure 1-1-2. CO_2 emission reduction potential by technology in Reference Case and REmap, 2010 – 2050.[3]

1-2 Lithium-Ion Batteries

Lithium-ion batteries (LIBs) are the most promising energy storage devices for BESS because of their high energy density and cycle stability.[6,7] They have been already widely used for various portable electronic devices, electric vehicles, thus they are mature and reliable from a technological perspective. LIBs typically consist of four major parts: cathode, anode, separator, and electrolyte. Their cathodes and anodes typically consist of lithium-cobalt-oxide ($LiCoO_2$) and graphitie, respectively.[7,8] The working mechanism of typical LIBs is shown in Figure 1-2-1(a). During charging process, Li^+ deintercalates from the cathode material and intercalates into the anode material. On the other hand, the reverse reactions occur during discharge process. There are four types of cells in LIBs: cylindrical, prismatic, coin, and pouch cell (Figure 1-2-1(b)-(e)). In practical, hundreds to thousands of cells are combined in parallel and/or in

series into modules and they form battery packs to obtain specific voltage and capacity (Figure 1-2-1(f)).

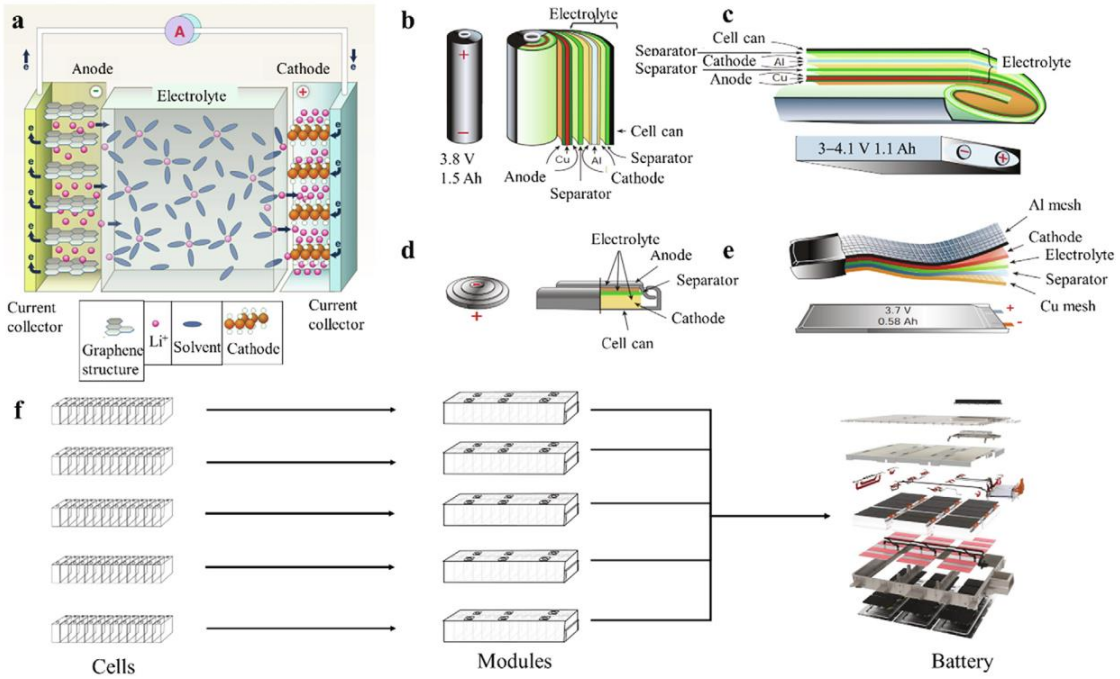

Figure 1-2-1. (a) Schematic diagram of the fundamental structure of a LIB cell, which is the same for different cell types. Cell types; (b) cylindrical cell; (c) prismatic cell; (d) coin cell; (e) pouch cell. (f) Schematic diagram of the relationship between cell, module, and battery.[9]

The specific capacity of LIBs is mainly limited by cathode active materials because the capacity of cathode active materials is much smaller than that of anode active materials (Figure 1-2-2). Therefore, various types of cathode active materials have been explored because increasing the capacity of the cathode active material leads to an increase in the overall capacity of the LIB cells. In addition, safety and environmental friendliness are required for active materials. $LiCoO_2$ cathodes have thermal runaway risk due to uncontrollable side reactions.[10] There is a large concern on environmental

footprint[11] and resource depletion of lithium metal and transition metal such as cobalt and nickel.[12] Cobalt and nickel are toxic to the environment and humans.[8] Vigorous studies on LIBs recycling have already begun for recycling the heavy metals in the cathode thorough chemical, bioleaching, and physical methods,[12,13] however, alternative cathode active materials have been explored to overcome these issues.[14,15]

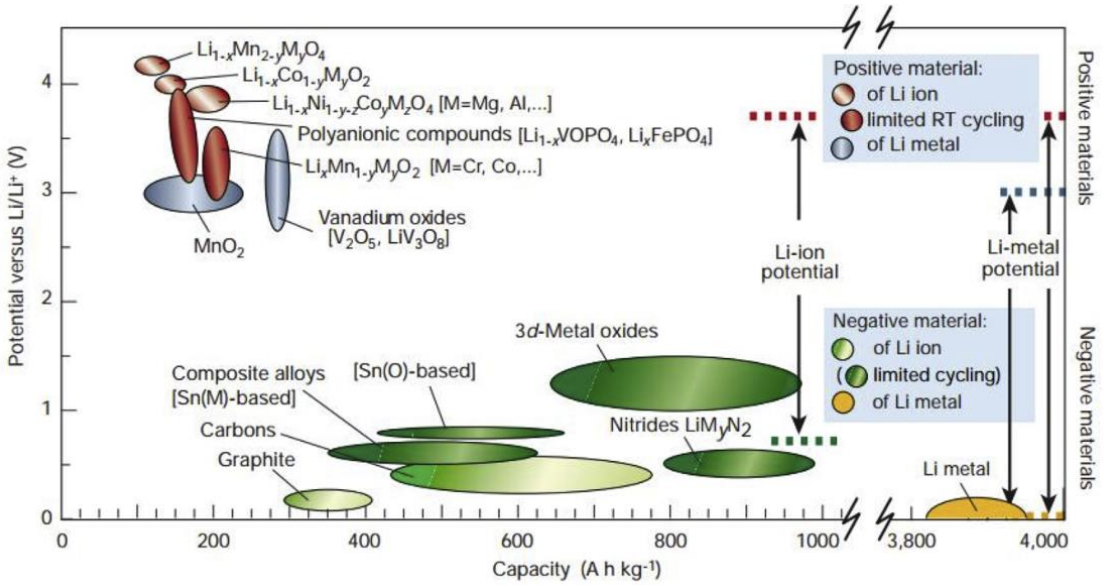

Figure 1-2-2. Electrode materials presently used or under serious considerations for rechargeable lithium-based batteries.[16]

1-3 Organic Active Cathode Materials for Lithium-Ion Batteries

Organic cathode active materials have attracted much attention as promising alternative cathode active materials for LIBs due to their environment-friendly nature, abundant resource, high specific capacity, and high safety.[17–25] Redox-active organic compounds are composed of abundant resources such as carbon, hydrogen, oxygen, nitrogen, and sulfur. They are not relying on the scarce transition metal resources owing to their chemical diversity and functional versatility. Since the first demonstration of the

prototype organic rechargeable battery in 1969 utilizing dichloroisocyanuric acid, a series of other redox-active organic electrode materials have been discovered as shown in Figure 1-3-1. Various types of organic redox-active compounds have been introduced in the past decades, for example, carbonyl compounds, nitrile compounds, organosulfur compounds, and radical polymers.

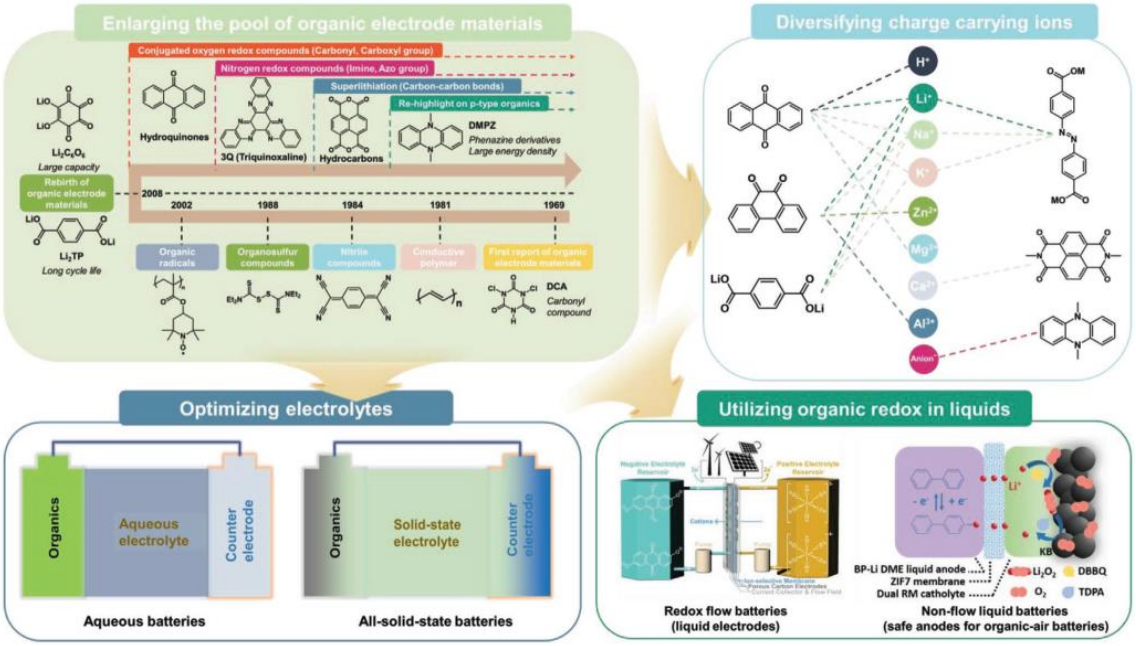

Figure 1-3-1. Paradigm shift in the utilization of redox-active organic compound in ESSs.[18]

There are three types by classifying the polarization: n-types, p-types, and bipolar-types. Also, they are classified into six categories of reactions by the functional groups as shown in Figure 1-3-2.[26] Among them, organic radicals exhibit the anion insertion reaction which have advantages of fast kinetics, high potential as cathodes.[17,27] Radical polymers with redox-active center of 2,2,6,6-tetramethylpiperidin-1-oxyl (TEMPO) are the most popular as an organic radical active material.[28–31] Because TEMPO itself

possesses high solubility in the electrolyte, polymer backbones are employed to bind the TEMPO to suppress dissolution into the electrolyte. However, it causes decrease of specific capacity because the polymer chain does not contribute redox reaction. Several other types of organic radical cathode active materials are proposed as shown in Figure 1-3-3.

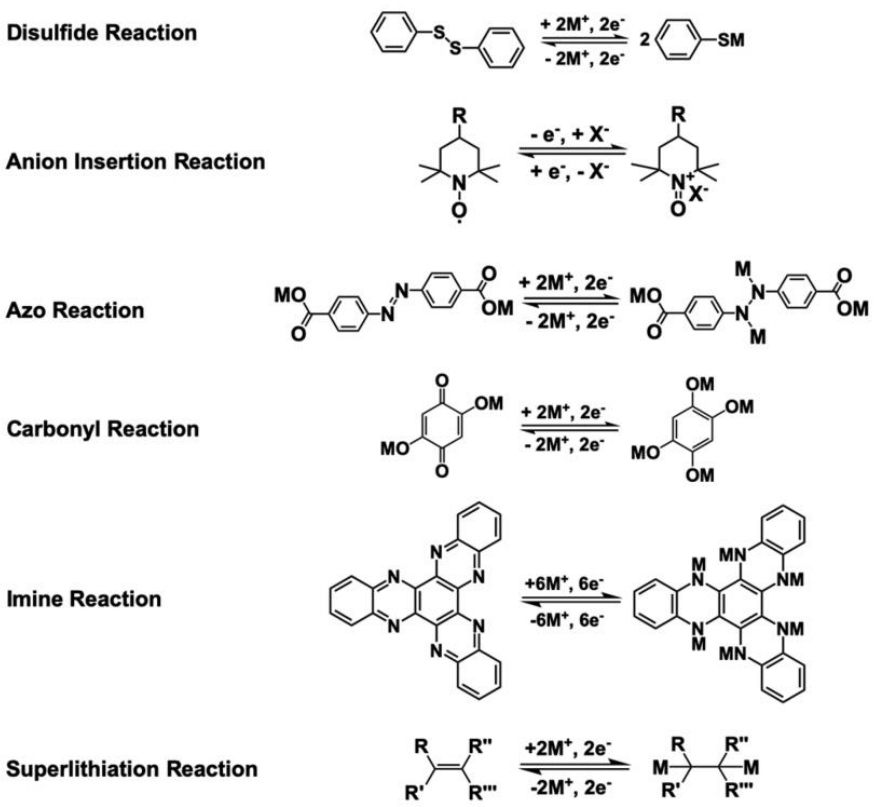

Figure 1-3-2. Reaction mechanisms of the organic electrode materials in organic batteries (M^+ = metal ions).[26]

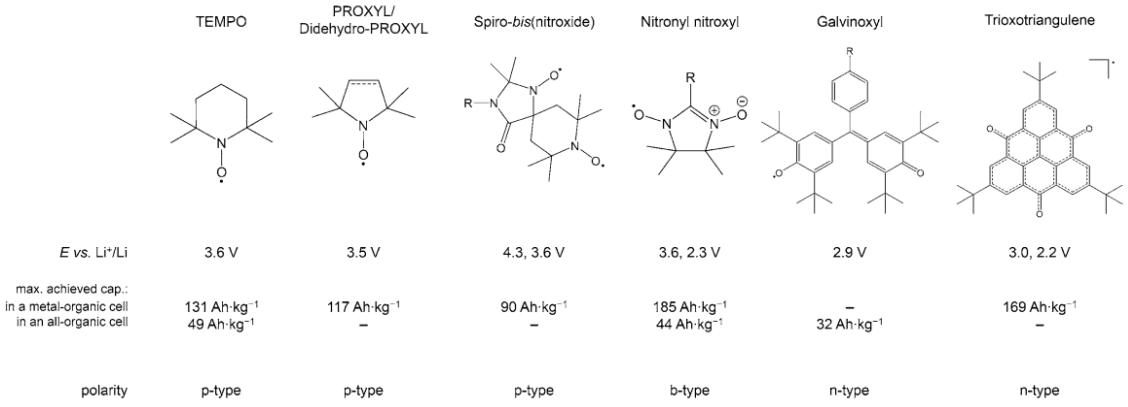

Figure 1-3-3. Overview on the molecular structures and key properties of the active radical materials.[27]

1-4 Trioxotriangulene: A Stable Neutral Organic π-Radical

Trioxotriangulene (TOT) is a stable organic neutral radical which possesses an electronic-spin structure delocalized on a 25π-electronic system.[32] TOT is one of the promising candidates as a high-capacity organic cathode active material due to their four-stage reversible redox ability from the neutral radical to radical tetraanion species.[33,34] Figure 1-4-1(a) shows molecular structure and multistage redox process of pristine TOT (H_3TOT). H_3TOT possesses a quite high theoretical capacity of 334 mA h g^{-1}, assuming that four electrons are involved in the charge/discharge process. TOT neutral radicals show extremely high stability in both solid and solution states even without steric protection groups, where the H_3TOT neutral radical is not decomposed even at 350°C under air or nitrogen atmosphere.[35] TOT derivatives generally form one-dimensional π-stacking columns due to their strong intermolecular interaction of singly occupied molecular orbitals (SOMO) and exhibit high electrical conductivities as a single component neutral radical.[36] Figure 1-4-1(b) shows one-dimensional π-stacking column of H_3TOT neutral radical crystals. The c-axis is along to π-π stacking direction.

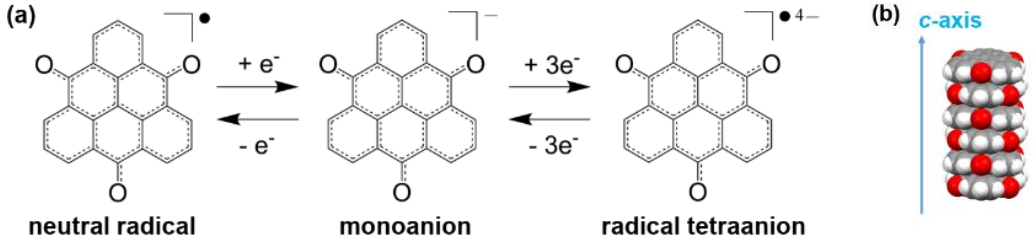

Figure 1-4-1. (a) Molecular structure and redox process of pristine trioxotriangulene (H_3TOT). (b) One-dimensional π-stacking column of H_3TOT neutral radical crystals.

Recently, Ito *et al.* successfully prepared orientation-controlled thin films of H_3TOT neutral radical using physical vapor deposition and evaluated their anisotropic conductivity.[37] Figure 1-4-2 shows schematic images of molecular orientations in the thin films of H_3TOT. The anisotropic orientation of the 1D columns depended on the substrates; edge-on-oriented thin films were obtained on glass, SiO_2, and indium-tin-oxide (ITO) substrates, whereas face-on oriented thin films were achieved on the graphite (0001) surface of highly oriented pyrolytic graphite (HOPG) and graphite sheets. The electrical conductivity of the edge-on oriented thin films showed high anisotropy; the electrical conductivity in the direction parallel to the substrate was considerably higher than that in the direction perpendicular to the substrate (10^{-2} vs 10^{-5} S cm^{-1}). These results indicate that c-axis epitaxial growth with face-on orientation occurs due to π-π interaction between the molecule and the substrate and high electrical conductivity along c-axis exhibits. Besides, Murata *et al.* successfully demonstrated vapor-deposited thin films of H_3TOT as a cathode without using any binder or conductive additive.[38] Figure 1-4-3 shows battery performances of the vapor-deposited films of H_3TOT neutral radical. The battery performance of the thin film cathodes was dependent on the molecular orientation; the face-on film exhibited higher rate and cycle performance than the edge-on film as shown in Figure 1-4-3(c), (d), (e), and (f). This result indicates that structural characteristics including the orientation of TOT on the graphite are a key factor in the performance of the redox reaction.

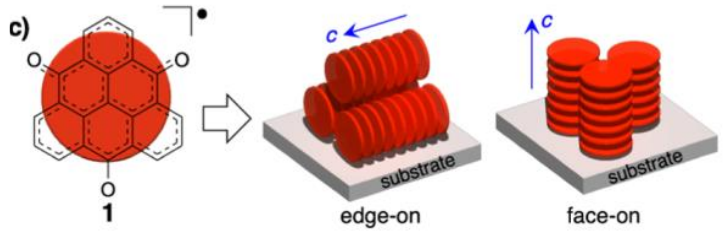

Figure 1-4-2. Schematic images of molecular orientations in the thin films of H_3TOT.[37]

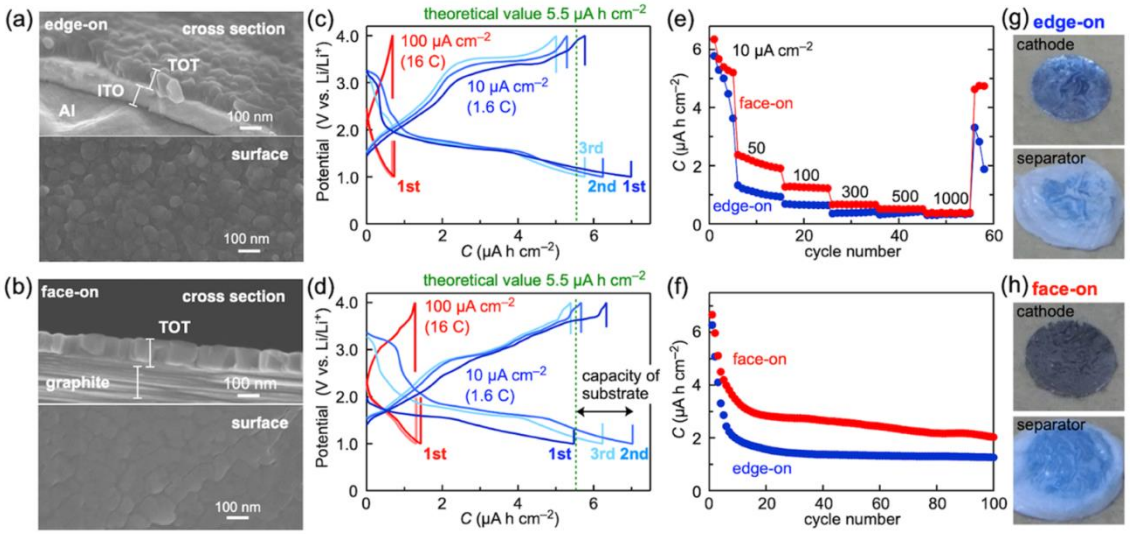

Figure 1-4-3. Battery performances of the vapor-deposited films of H_3TOT neutral radical. (a, b) SEM images of vapor-deposited thin films on ITO/Al (edge-on) and graphite 0001 (face-on) substrates, respectively. (c, d) Charge/discharge processes of coin-type cells using 100 nm thick edge-on and face-on films, respectively, at current densities of 10 μA cm^{-2} (blue) and 100 μA cm^{-2} (red). (e) Rate performance of edge-on (blue) and face-on (red) orientations at current densities of 10 – 1000 μA cm^{-2}. (f) Cycle performance at current densities of 10 μA cm^{-2}. (g, h) Photographs of the cell components after 100 charge/discharge cycles at a current density of 10 μA cm^{-2}.[38]

Despite the advantages of TOT as an organic cathode active material, capacity degradation upon repeated charge/discharge cycles is a critical issue for organic radical batteries. For TOT cathodes in carbonate-based electrolyte solutions, their capacity degradation is mainly caused by the dissolution and/or deformation of TOT microcrystals with the charge/discharge.[34,38] In fact, the separators of the cell after the battery test were stained with deep blue H_3TOT anion salts dissolved in the electrolyte solution as shown in Figure 1-4-3(g) and (h). This is because the solubility of TOT is drastically changed by different valence states; the neutral radical is not dissolved, whereas the anion species is easily dissolved in common organic solvents including a carbonate-based electrolyte.

The cycle degradation caused by the dissolution is also observed in quinone- and tetracyanoquinodimethane-based species especially of low molecular weight[17,39] and even in some redox polymers.[40,41] Kolek *et al.* discussed the cycling behavior and solubility properties of a polyvinyl-based redox polymer with a methylphenothiazine side group (PVMPT) in organic-solvent-based battery electrolytes by post-reaction electrode surface investigations via microscopy and X-ray photoelectron spectroscopy.[40] Figure 1-4-4 shows the schematic image of the mechanism of charge/discharge of a PVMPT-based electrode. The solubility of PVMPT is dependent on the oxidation states; PVMPT in the oxidized state **C** is dissolved, whereas that in neutral state **A** and semioxidized state **B** is not dissolved in the carbonate-based electrolyte solution. During the first charge process, PVMPT is oxidized to the state **C** and partially dissolved in the electrode. Upon discharge, the polymer was reduced to a mixture of two states **A** and **B** and redeposited onto and in the carbon network. As cycle numbers increased, PVMPT was only reduced to the state **B**, while **A** was not recovered anymore. This mechanism

indicates that the loss of active material does not have to be entirely irreversible, and that stable cycling behavior can be achieved despite dissolution. Meanwhile, in the TOT cathode system, the redox and structural behavior of the molecules dissolved into or redeposited from the electrolyte solution are still unclear.

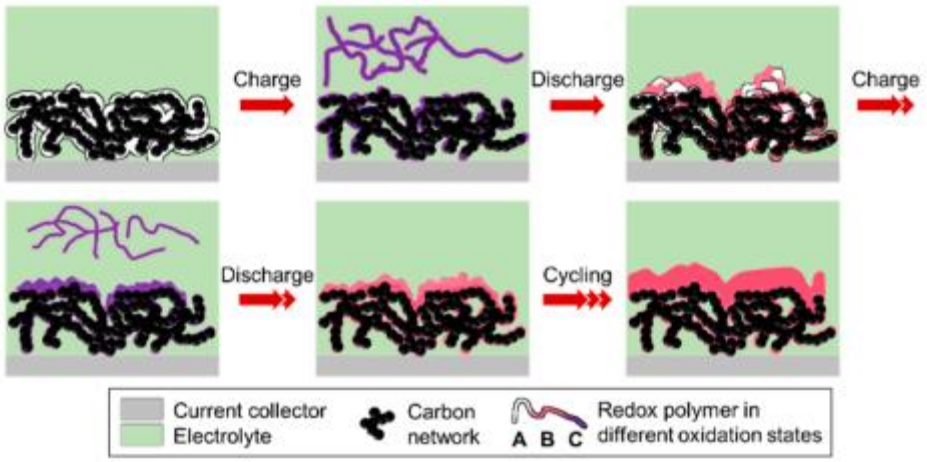

Figure 1-4-4. Schematic image of the mechanism of charge/discharge of a PVMPT-based electrode.[40]

1-5 *In Situ* Analyses at the Interface of Electrolyte/Active Materials

In situ analyses of redox-active materials under electrochemical conditions are significant to elucidate fundamental and microscopic mechanisms of an electron transfer and a structural change. They have been intensely performed using *in situ* scanning probe microscopy or spectroscopy.[42,43] Utsunoimya *et al*. reported a correlation between the electrochemical reactivity and the molecular aggregate structure of bisphenalenyl diradical, tetra *tert*-butyl derivatives of s-indacenodiphenalene (TTB-IDPL), adsorbed on a highly oriented pyrolytic graphite (HOPG) electrode surface in aqueous electrolyte by *in situ* frequency modulation atomic force microscopy.[44,45] As shown in Figure 1-5-1, the change in the morphology was due to the applied electrode potential in the redox-incactive range (Figure 1-5-1(a)-(g)), and only the molecules directly attached to the graphite electrode, whose portion was irreversibly increased by the potential application, became redox-active (Figure 1-5-1(h)). Morino *et al.* reported an asymmetric lithiation/delithiation mechanism of 1,4-benzoquinone by investigating redox processes of its self-assembled monolayer (SAM) on a gold electrode via operando shell-isolated nanoparticle enhanced Raman spectroscopy.[46] These new insights of microscopic electrochemical behavior at electrode/electrolyte interface through *in situ* analyses will likely lead to a better understanding of redox mechanisms and structural changes and to an optimized electrode design in organic rechargeable batteries.

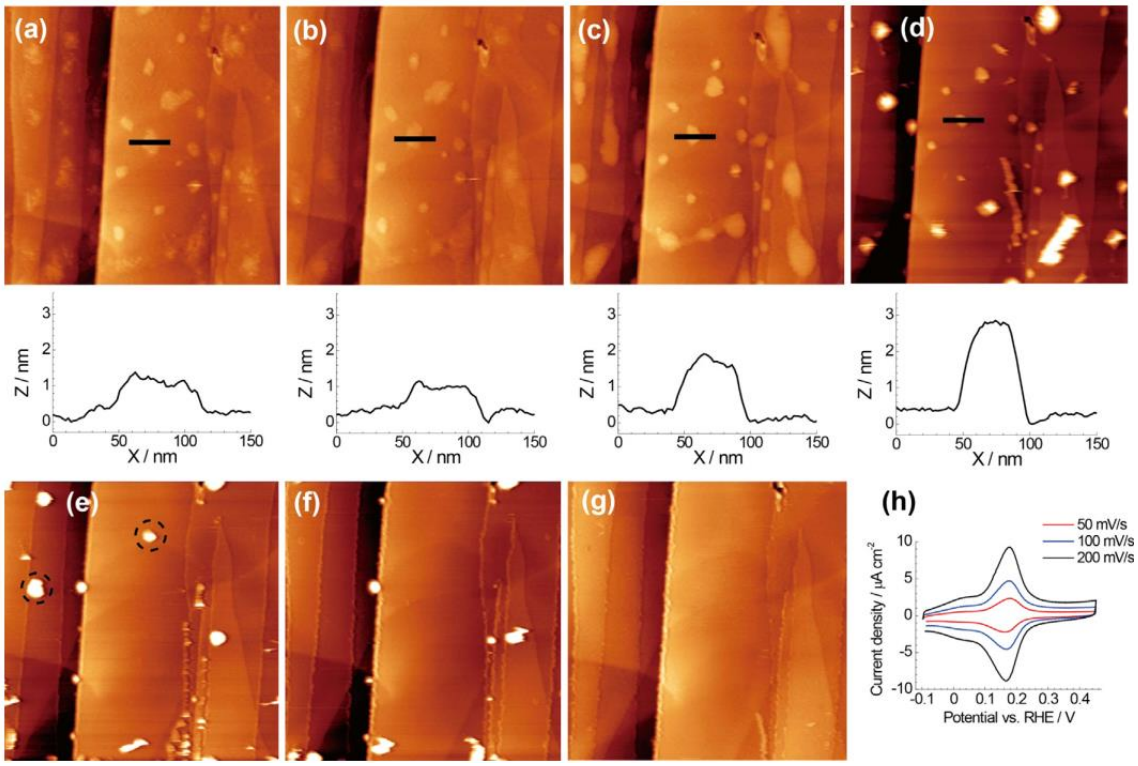

Figure 1-5-1. Series of *in situ* FM-AFM images of a TTB-IDPL film on an HOPG electrode and topographic line profiles of a molecular aggregate in 0.1 M $HClO_4$ at different electrode potentials; (a) −0.02 V, (b) 0.48 V, (c) 0.88 V, and (d) 1.28 V. (e, f) Consecutively scanned images at 1.78 V. (g) An FM-AFM image after applying the anodic potential of 1.78 V. (h) Steady state cyclicvoltammograms of TTB-IDPL adsorbed on HOPG electrodes in 0.1 M $HClO_4$, which was obtained after several potential scans in the range between 0.1 and 1.4 V.[45]

Infrared (IR) spectroscopy is a powerful surface-sensitive technique for probing the chemical species and molecular orientation on solid surfaces,[47–50] and *in situ* IR spectroelectrochemistry have been used to investigate the near-surface structure of the electrode/electrolyte interface. However, difficulties may arise from the strong IR absorption of the electrolyte in external reflection geometry, which usually masks the IR

signal of the surface species. To enhance its interfacial sensitivity, certain techniques are proposed and may be applied for *in situ* IR measurements including IR attenuated total reflectance (ATR) spectroscopy,[51,52] subtractively normalized interfacial Fourier transform IR spectroscopy (SNIFTIRS),[53,54] polarization modulation reflection-absorption spectroscopy (PM-IRRAS),[55,56] surface-enhanced IR absorption spectroscopy (SEIRAS).[57] For example, Han *et al.* revealed the formation process and structure of a SAM of lipoic-acid terminated polyproline (Lip-G-P_{15}-W-NH_2) on a gold surface in aqueous solutions by *in situ* IR ATR spectroelectrochmistry in the polarized IR ATR configuration (Figure 1-5-2).[52] Therefore, *in situ* IR spectroelectrochemistry is suitable for investigating redox mechanisms associated with structural and/or orientation change.

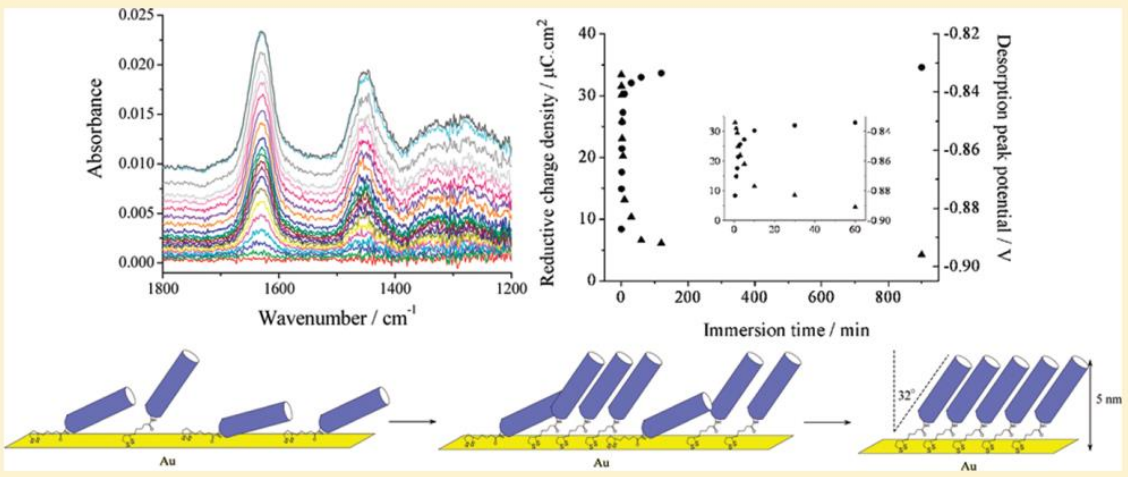

Figure 1-5-2. (Top left) IR spectra of the gold surface during the absorption process in 1 μM Lip-G-P_{15}-W-NH_2 D_2O solution. (Top right) Immersion time dependencies of reductive charge density and deposition peak potential of SAM prepared in 10 μM Lip-G-P_{15}-W-NH_2 D_2O solution. (Bottom) Schematic model of the formation process of Lip-G-P_{15}-W-NH_2 SAM on a gold surface in Lip-G-P_{15}-W-NH_2 D_2O solution.[52]

Here, we present voltammetric and *in situ* IR spectroelectrochemical studies on TOT on a graphite electrode in a non-aqueous electrolyte. This is the first report on *in situ* IR spectroelectrochemistry of TOT derivatives on the graphite electrode surfaces. This study allows us to discuss the microscopic electrochemical dynamics of TOT on the graphite surfaces.

1-6 Scope of This Dissertation

This dissertation consists of six chapters. Chapter 1 provides general introduction to this doctoral dissertation research. Chapter 2 is a review on the principles and techniques related to this dissertation. In Chapter 3, electrochemical measurements and electron microscopy analyses of TOT on the graphite electrode surface were performed to investigate the redox behaviors and structural changes. In Chapter 4, mechanistic investigations of the electrochemical dynamics of TOT on the graphite electrode surface were performed by *in situ* IR spectroelectrochemistry. Chapter 5 provides a summary of the significance of the results, the achievement of this dissertation, and the future prospects. More details of Chapter 3 and 4 are summarized as follows.

Chapter 3. ***Electrochemical Behaviors and Structural Changes During the Redox Processes of Trioxotriangulene on Graphite Electrode Surfaces***

To investigate the electrochemical behaviors of TOT at the graphite electrode/non-aqueous electrolyte interface, voltammetric measurements on graphite sheet electrodes in non-aqueous electrolyte solutions containing TOT monoanion were performed. The redox reversibility between monoanion and neutral radical species were dependent on the concentration of TOT monoanion and repeating cycle of the redox process. The

electron microscopic analyses of the post-reaction electrodes revealed that the deposition and dissolution of TOT neutral radical crystals occurred with oxidation and reduction process. The results suggested that the redox activity of TOT neutral radical crystals on the graphite electrode surface was dependent on its orientation; the crystals of face-on alignment were reducible and dissolvable whereas those of edge-on were not. A preliminary model of electrochemical and structural behavior on the redox processes of TOT on the graphite electrode surface was proposed.

Chapter 4. ***Mechanistic Investigations on the Redox Processes of Trioxotriangulene on the Graphite Electrode Surface by In Situ Infrared Spectroelectrochemistry***

Prior to *in situ* IR spectroelectochemistry, FT-IR characterization of TOT neutral radical species was performed by *ex situ* reflection-absorption (RA) spectroscopy of the post-reaction electrodes quenched at different potentials. The characterization of absorption bands and vibration orientations were performed by comparing to an ATR spectrum of as-synthesized powder and DFT calculations. Consequently, *in situ* IR ATR spectroelectrochemical analyses were performed to investigate microscopic dynamics of the redox processes of TOT on the graphite electrode surface. The analyses successfully confirmed the alignments of the edge-on and the face-on alignments of the TOT neutral radicals in the crystal at different electrochemical potentials. The results basically supported the model proposed in Chapter 3. In addition, one of the possible origins of the irreversible redox process was confirmed. Finally, a schematic concept of the oxidation/reduction process accompanied by deposition/dissolution of TOT on the graphite surface was proposed.

References

1. United Nations Department of Economic and Social Affairs (UN DESA), "THE 17 GOALS | Sustainable Development," https://sdgs.un.org/goals, **2017**.
2. D. Gielen, F. Boshell, D. Saygin, M. D. Bazilian, N. Wagner, R. Gorini, *Energy Strateg. Rev.* **2019**, *24*, 38.
3. IRENA, *Global Energy Transformation: A Roadmap to 2050*, **2019**.
4. Y. Yang, S. Bremner, C. Menictas, M. Kay, *Renew. Sustain. Energy Rev.* **2018**, *91*, 109.
5. M. A. Hannan, A. Q. Al-Shetwi, R. A. Begum, P. Jern Ker, S. A. Rahman, M. Mansor, M. S. Mia, K. M. Muttaqi, Z. Y. Dong, *J. Energy Storage* **2021**, *42*, 103040.
6. B. Diouf, R. Pode, *Renew. Energy* **2015**, *76*, 375.
7. B. Dunn, H. Kamath, J. M. Tarascon, *Science* **2011**, *334*, 928.
8. M. Li, J. Lu, Z. Chen, K. Amine, *Adv. Mater.* **2018**, *30*, 1800561.
9. Y. Chen, Y. Kang, Y. Zhao, L. Wang, J. Liu, Y. Li, Z. Liang, X. He, X. Li, N. Tavajohi, B. Li, *J. Energy Chem.* **2021**, *59*, 83.
10. K. Liu, Y. Liu, D. Lin, A. Pei, Y. Cui, *Sci. Adv.* **2018**, *4*, eaas9820.
11. M. Wentker, M. Greenwood, M. C. Asaba, J. Leker, *J. Energy Storage* **2019**, *26*, 101022.
12. D. L. Thompson, J. M. Hartley, S. M. Lambert, M. Shiref, G. D. J. Harper, E. Kendrick, P. Anderson, K. S. Ryder, L. Gaines, A. P. Abbott, *Green Chem.* **2020**, *22*, 7585.
13. B. Huang, Z. Pan, X. Su, L. An, *J. Power Sources* **2018**, *399*, 274.
14. G. E. Blomgren, *J. Electrochem. Soc.* **2017**, *164*, A5019.

15. T. Kim, W. Song, D. Y. Son, L. K. Ono, Y. Qi, *J. Mater. Chem. A* **2019**, *7*, 2942.

16. Q. Li, J. Chen, L. Fan, X. Kong, Y. Lu, *Green Energy Environ.* **2016**, *1*, 18.

17. C. Friebe, A. Lex-Balducci, U. S. Schubert, *ChemSusChem* **2019**, *12*, 4093.

18. S. Lee, J. Hong, K. Kang, *Adv. Energy Mater.* **2020**, *10*, 2001445.

19. S. B. Xia, T. Liu, W. J. Huang, H. B. Suo, F. X. Cheng, H. Guo, J. J. Liu, *J. Energy Chem.* **2020**, *51*, 303.

20. C. Peng, G. H. Ning, J. Su, G. Zhong, W. Tang, B. Tian, C. Su, D. Yu, L. Zu, J. Yang, M. F. Ng, Y. S. Hu, Y. Yang, M. Armand, K. P. Loh, *Nat. Energy* **2017**, *2*, 1.

21. K. C. Kim, *Ind. Eng. Chem. Res.* **2017**, *56*, 12009.

22. M. Lee, J. Hong, H. Kim, H. D. Lim, S. B. Cho, K. Kang, C. B. Park, *Adv. Mater.* **2014**, *26*, 2558.

23. Y. Lu, Y. Cai, Q. Zhang, J. Chen, *Adv. Mater.* **2022**, *34*, 2104150.

24. D. Xu, M. Liang, S. Qi, W. Sun, L. P. Lv, F. H. Du, B. Wang, S. Chen, Y. Wang, Y. Yu, *ACS Nano* **2021**, *15*, 47.

25. K. Qin, J. Huang, K. Holguin, C. Luo, *Energy Environ. Sci.* **2020**, *13*, 3950.

26. J. J. Shea, C. Luo, *ACS Appl. Mater. Interfaces* **2020**, *12*, 5361.

27. C. Friebe, U. S. Schubert, *Top. Curr. Chem.* **2017**, *375*, 1.

28. K. Nakahara, K. Oyaizu, H. Nishide, *Chem. Lett.* **2011**, *40*, 222.

29. T. Suga, H. Ohshiro, S. Ugita, K. Oyaizu, H. Nishide, *Adv. Mater.* **2009**, *21*, 1627.

30. K. Nakahara, S. Iwasa, M. Satoh, Y. Morioka, J. Iriyama, M. Suguro, E. Hasegawa, *Chem. Phys. Lett.* **2002**, *359*, 351.

31. K. Oyaizu, H. Nishide, *Adv. Mater.* **2009**, *21*, 2339.

32. Y. Morita, S. Suzuki, K. Sato, T. Takui, *Nat. Chem.* **2011**, *3*, 197.

33. Y. Morita, S. Nishida, T. Murata, M. Moriguchi, A. Ueda, M. Satoh, K. Arifuku, K. Sato, T. Takui, *Nat. Mater.* **2011**, *10*, 947.

34. H. Ito, T. Murata, M. Fujisaki, R. Tsuji, Y. Morita, *ChemSusChem* **2021**, cssc.202002851.

35. Y. Morita, T. Murata, A. Ueda, C. Yamada, Y. Kanzaki, D. Shiomi, K. Sato, T. Takui, *Bull. Chem. Soc. Jpn.* **2018**, *91*, 922.

36. T. Murata, C. Yamada, K. Furukawa, Y. Morita, *Commun. Chem.* **2018**, *1*, 47.

37. H. Ito, T. Murata, T. Miyata, M. Morita, R. Tsuji, Y. Morita, *ACS Omega* **2019**, *4*, 17569.

38. T. Murata, S. Nakanishi, H. Nakayama, H. Ito, M. Morita, R. Tsuji, Y. Morita, *ACS Appl. Energy Mater.* **2022**, *5*, 1218.

39. M. Yao, S. I. Yamazaki, H. Senoh, T. Sakai, T. Kiyobayashi, *Mater. Sci. Eng. B Solid-State Mater. Adv. Technol.* **2012**, *177*, 483.

40. M. Kolek, F. Otteny, J. Becking, M. Winter, B. Esser, P. Bieker, *Chem. Mater.* **2018**, *30*, 6307.

41. J. Kim, J. H. Kim, K. Ariga, *Joule* **2017**, *1*, 739.

42. K. Yamamoto, T. Minato, S. Mori, D. Takamatsu, Y. Orikasa, H. Tanida, K. Nakanishi, H. Murayama, T. Masese, T. Mori, H. Arai, Y. Koyama, Z. Ogumi, Y. Uchimoto, *J. Phys. Chem. C* **2014**, *118*, 9538.

43. P. P. R. M. L. Harks, F. M. Mulder, P. H. L. Notten, *J. Power Sources* **2015**, *288*, 92.

44. T. Utsunomiya, Y. Yokota, T. Enoki, Y. Hirao, T. Kubo, K. Fukui, *Carbon* **2013**, *63*, 196.

45. T. Utsunomiya, Y. Yokota, T. Enoki, Y. Hirao, T. Kubo, K. Fukui, *Carbon* **2014**, *77*, 184.

46. Y. Morino, K. Fukui, *Langmuir* **2022**, *38*, 3951.

47. T. Hasegawa, T. Koganezawa, N. Shioya, K. Nakao, T. Shimoaka, H. Yoshida, K. Eda, R. Murdey, *Sci. Rep.* **2019**, *9*, 1.

48. T. Nakamura, N. Shioya, T. Shimoaka, R. Nishikubo, T. Hasegawa, A. Saeki, Y. Murata, R. Murdey, A. Wakamiya, *Chem. Mater.* **2019**, *31*, 1729.

49. N. Shioya, R. Fujiwara, K. Tomita, T. Shimoaka, T. Hasegawa, *J. Phys. Chem. A* **2020**, *124*, 2714.

50. F. Anariba, U. Viswanathan, D. F. Bocian, R. L. McCreery, *Anal. Chem.* **2006**, *78*, 3104.

51. A. Davantès, G. Lefèvre, *Surf. Sci.* **2016**, *653*, 88.

52. Y. Han, H. Noguchi, K. Sakaguchi, K. Uosaki, *Langmuir* **2011**, *27*, 11951.

53. S. N. Port, D. J. Schiffrin, T. Solomon, *Langmuir* **1995**, *11*, 4577.

54. J. Zhang, F. C. Anson, *J. Electroanal. Chem.* **1992**, *331*, 945.

55. L. Vieira, R. Schennach, B. Gollas, *Phys. Chem. Chem. Phys.* **2015**, *17*, 12870.

56. M. Bieri, T. Bürgi, *J. Phys. Chem. B* **2005**, *109*, 22476.

57. Z. Li, B. Han, G. Meszaros, I. Pobelov, T. Wandlowski, A. Błaszczyk, M. Mayor, *Faraday Discuss.* **2006**, *131*, 121.

Chapter 2
Principles and Techniques

2-1 Voltammetry

Electrochemistry is a powerful technique for investigating chemical reactions involving electron transfers. Voltammetry is one of the electrochemical methods. The electrochemical response can be obtained through a series of steps to different potentials with recording of the current-time curves to yield a three-dimensional current (*i*)-time (*t*)-potential (*E*) surface (Figure 2-1-1(a)). Votammetry (recording the current as a function of electrode potential) are often applied to obtain the electrochemical response in a single experiment. Linear sweep voltammetry (LSV) and cyclic voltammetry (CV) are very popular potential sweep techniques for initial electrochemical studies and very useful in obtaining information about complicated electrode systems.[1–7] Sweeping the potential linearly with time at a constant sweep rate and recording the *i*-*E* curve corresponds to traversing the three-dimensional *i*-*t*-*E* realm (Figure 2-1-1(b)).

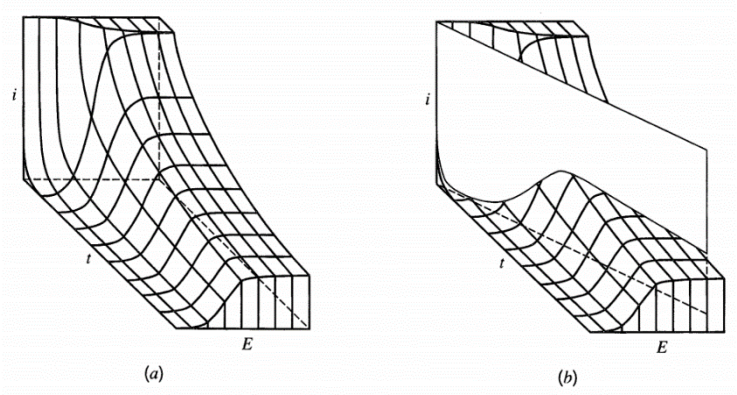

Figure 2-1-1. (a) A portion of the *i*-*t*-*E* surface for a Nernstian reaction. (b) Linear potential sweep across this surface.[7]

An experimental arrangement for voltammetric measurements is shown in Figure 2-1-2. An electrochemical cell consists of three electrodes; a working electrode, a counter electrode, and a reference electrode. In the three-electrode system, a potentiostat

controls the voltage across the working electrode-counter electrode pair, and it adjusts this voltage to maintain the potential difference between the working and reference electrodes. Since the current and the potential are functionally related, the observed current corresponds to the flow of electrons needed to support the active electrochemical processes at a rate consistent with the potential.

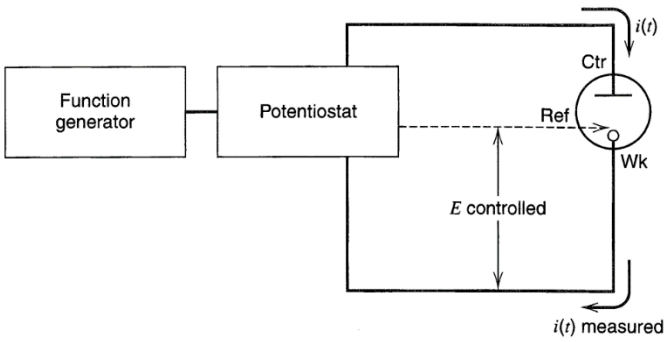

Figure 2-1-2. An experimental arrangement for controlled-potential experiments.[7]

As an example, let us consider the LSV response of the anthracene in dimethylformamide (DMF) as a typical redox active system, which is shown in Bard's book.[7] Suppose the scan is begun at an initial potential E_i in a negative direction at a constant scan rate (Figure 2-1-3(a)). If the scan is begun at a potential well positive of $E^{0'}$ for the reduction, only non-faradaic currents flow for a while. When the electrode potential reaches the vicinity of $E^{0'}$, the reduction from neutral **A** to anion radical $\mathbf{A}^{\cdot-}$ begins. At this moment, the faradaic current starts to flow. As the potential moves past $E^{0'}$, the surface concentration of **A** drops nearly to zero, causing the current to peak. The current then decays due to diffusion-limited rate. As a result, the observed LSV curve for this system is like that shown in Figure 2-1-3(b). At the fully cathodic potential, the concentration profiles near the electrode are like those shown in Figure 2-1-3(c).

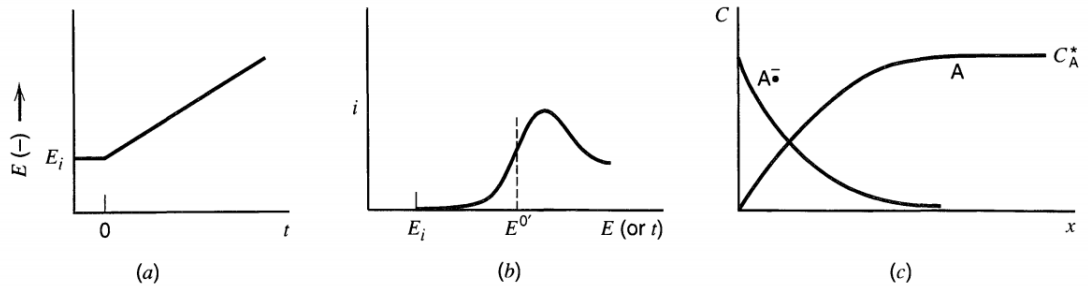

Figure 2-1-3. (a) Linear potential sweep starting at E_i. (b) Resulting LSV curve. (c) Concentration profiles of $\mathbf{A}^{\bullet-}$ and **A** for potentials beyond the peak.[7]

Next, let us consider the cyclic potential sweep that the potential scan is reversed at the potential E_λ (at the switching time λ) as shown in Figure 2-1-4(a). At the switching potential E_λ, there is a large concentration of the oxidizable anion radical $\mathbf{A}^{\bullet-}$ in the vicinity of the electrode surface. As the potential approaches, then passes, $E^{0'}$, the anion radical becomes oxidized to neutral species and anodic currents flow. This reversal current has a shape like that of forward peak for the same reasons. As a result, the observed CV curve is like that shown in Figure 2-1-4(b).

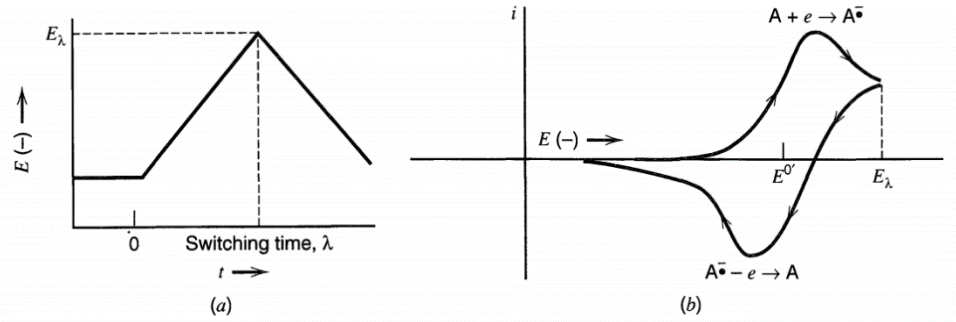

Figure 2-1-4. (a) Cyclic potential sweep. (b) Resulting cyclic voltammogram.[7]

The number of electrons involved in the redox reaction can be calculated by integrating the faradaic current with respect to time (Faraday's law), which corresponds

to the peak area of a voltammogram at a constant sweep rate.[8,9] The shape of a voltammogram indicates the information about the reversibility of the electrochemical system and the kinetic parameter can be evaluated by varying scan rate.[10,11]

Redox properties of TOT derivatives can be discussed by measuring cyclic voltammetry of the monoanion species in an electrolyte solution. Morita *et al.* reported redox behaviors of TOT derivatives with different substituents by cyclic voltammetry of the corresponding monoanion species in DMF solutions (Figure 2-1-5).[12] Pristine TOT (H_3TOT, **1**) exhibited four redox processes from neutral radical to radical tetraanion species (E^1 to E^4), where E^1 and E^4 were irreversible due to the low solubility, and E^2 and E^3 were reversible. The E^1 values of **3** (with electron-rich substituent groups) were significantly lower than that of **1**. In the case of **6** (halogenated derivatives), the electron-withdrawing ability of the substituent groups caused the positive shifts in the E^2-E^4 processes. In this dissertation, more detailed electrochemical behavior of TOT in the E^1 process on graphite electrode was investigated using voltammetry.

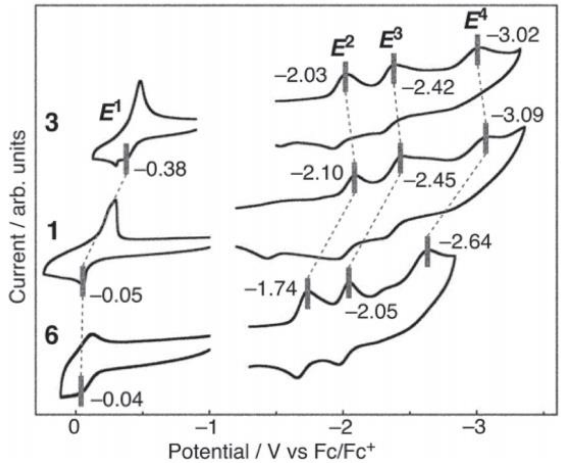

Figure 2-1-5. Cyclic voltammograms of H_3TOT (**1**), (n-BuO)$_3$TOT (**3**) and F_3TOT (**6**) measured using their n-Bu_4N^+ salts of monoanion species (5 mM) in DMF solution.[12]

2-2 Fourier Transform Infrared (FT-IR) Spectroscopy

2-2-1 Principle of FT-IR Spectroscopy

Fourier transform infrared (FT-IR) spectroscopy has been widely used for a range from the analysis of small molecules to the analysis of biological tissues.[13] IR spectroscopy probes the molecular vibration. The vibration is IR active if there is a change in the dipole moment associated with the molecular vibration. Functional groups have characteristic IR absorption bands corresponding to the fundamental vibrations. Characteristic vibrations of covalently bonded atoms can be classified as symmetric stretching, antisymmetric stretching, and bending as shown in Figure 2-2-1.

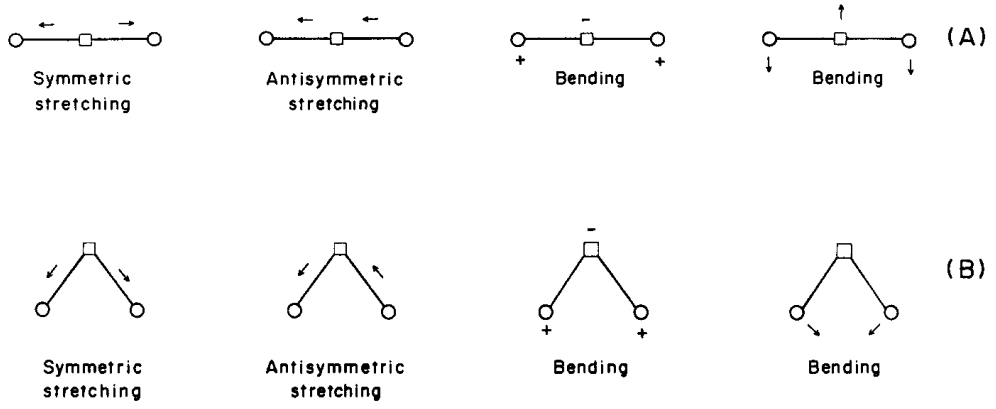

Figure 2-2-1 Types of normal vibration in a linear (A) and non-linear (B) triatomic molecule. Atomic displacements are represented by arrows (in-plane of page) and by + and – symbols (out-of-plane page).[14]

FT-IR spectrometers produce an interferometric pattern. The Michelson interferometer (Figure 2-2-2) is one of the most common instruments, which is composed of a beam-splitter (B) mounted at a 45° angle of incidence and two plane mirrors, a fixed one (F) and a moving one (M), placed with a 90° angle of incidence.[14] It

can divide a beam of radiation into two paths and then recombine the two beams after an optical path difference has been introduced by displacing the mirror M. The point where the distance BF is equal to BM is called the zero-path-difference (ZPD). The intensity of the light which reaches a detector will be a function of the distance travelled by M due to destructive interference depending on the optical path difference. A plot of intensity vs mirror displacement is called an interferogram (Figure 2-2-3). The interferometric data from this real space is then Fourier transformed into the frequency domain. The intensity vs frequency spectrum is obtained by subtracting the background spectrum from the single beam spectrum of the sample.

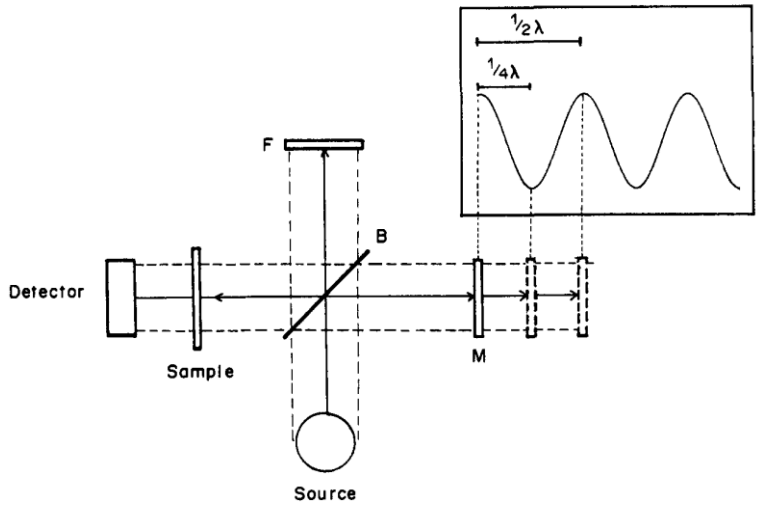

Figure 2-2-2 Schematic representation of a Michelson interferometer. Inset: representation of the resultant intensity at different optical retardation with a monochromatic light as a source.[14]

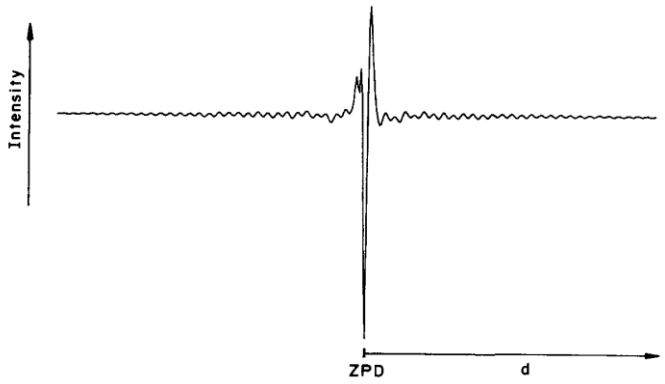

Figure 2-2-3 Double sided interferogram usually obtained in commercial instruments to perform phase correction. The zero-path difference (ZPD) point corresponds to the point of even symmetry and is the value where all frequencies interfere constructively.[14]

2-2-2 IR Reflection-Absorption (RA) Spectroscopy

IR RA spectroscopy is a powerful technique that provides the molecular orientation on a metallic substrate[15] involving HOPG[16] through the surface selection rule. IR light is incident at a grazing angle θ (typically 70 – 80°) on a sample in RA measurements. When IR light is incident on a metallic substrate, the incident electric field induces opposite image charges in the substrate (image charge effect). The s-polarized light (its electric field is parallel to the interface) is canceled out by the original electric field due to the image charge. (Figure 2-2-4(a)). In contrast, when p-polarized light (its electric field is perpendicular to the interface) is used, it has a large component perpendicular to the interface and a small component parallel to the interface because of the large incident angle. (Figure 2-2-4(b)). The electric field induced by the image charge and the original electric field reinforce each other, resulting in an electric field stronger than that of incident light. Conversely, the component parallel to the interface is cancelled out as well as s-polarized light. Therefore, only the transition moment component

perpendicular to the film surface selectively appears in an RA spectrum. This is called the surface selection rule of the RA spectroscopy.

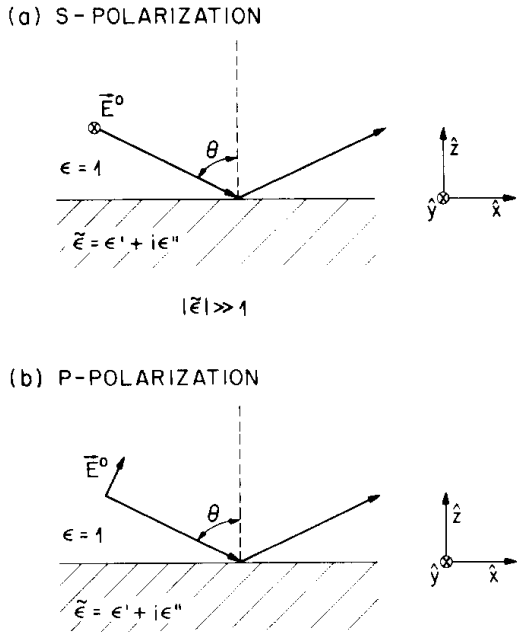

Figure 2-2-4 Schematic representation of a plane wave beam of radiation incident at angle θ onto a metallic or strongly absorbing substrate for the two polarizations of interest.[17]

Molecular orientation of thin film on a metallic substrate can be discussed by RA spectra due to the surface selection rule. Umemura *et al.* revealed the order-disorder transition occurring in the Langmuir-Blodgett (LB) film of Cd stearates with 9 monolayers on the silver-coated glass substrate by using RA spectroscopy (Figure 2-2-5).[18] At 31°C, asymmetric stretching vibration $\nu_a(CH_2)$ and symmetric stretching vibration $\nu_s(CH_2)$ bands appeared at 2917 and 2849 cm^{-1}, respectively, which indicated that the structure of the alkyl chain is ordered because each wavenumber is typical for the alkyl chain with all-trans conformation. These bands developed significantly above

105°C, indicating that the component of dipole moment perpendicular to the surface suddenly increased and the LB film became disordered at high temperatures. In this dissertation, RA spectroscopy was employed for FT-IR characterizations of TOT on a graphite electrode surface for following *in situ* IR spectroelectrochemistry.

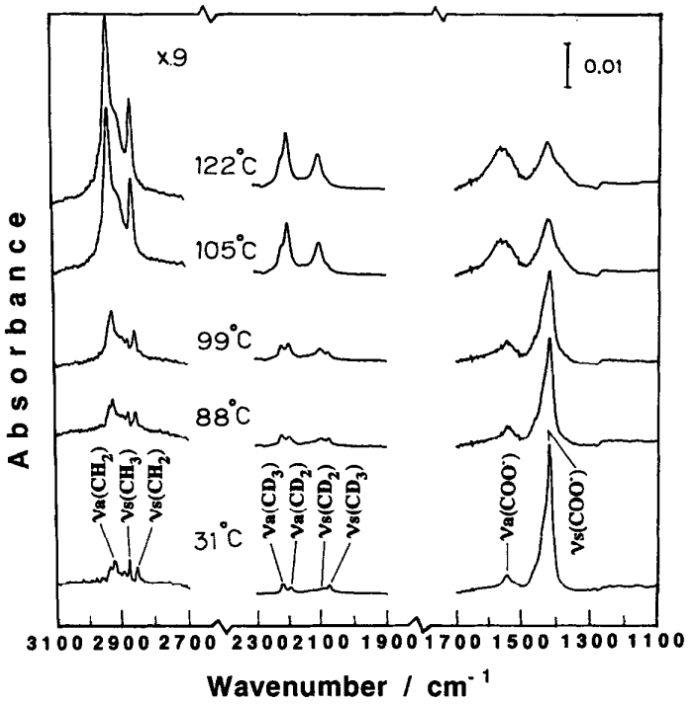

Figure 2-2-5. FT-IR RA spectra of 9-monolayer LB film of Cd stearate at elevated temperatures.[18]

2-2-3 IR Attenuated Total Reflection (ATR) Spectroscopy

IR ATR spectroscopy is also often applied for the interfacial analyses, which uses evanescent wave induced by total internal reflection. For angles of incidence greater than the critical angle, the incident light is passed through the ATR crystal (electric permittivity of ε) in such a way that it totally internally reflected (Figure 2-2-5). The sample is located in contact with the ATR crystal. The transmitted field into the sample (vacuum side in Figure 2-2-5) are evanescent. For an incident light of s-polarization, the

spectrum is dominated only by the component parallel to the surface (*y*-axis) (Figure 2-2-5(a)). On the other hand, for an incident light of p-polarization, the spectrum is a superposition of the component parallel and perpendicular to the surface (*x*-axis and *z*-axis) (Figure 2-2-5(b)).

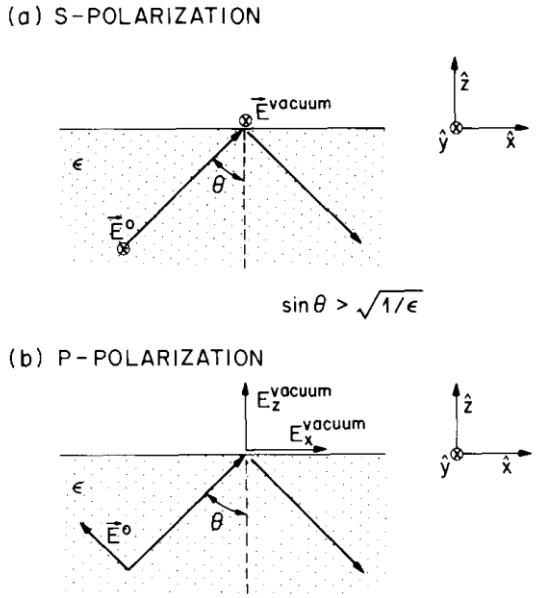

Figure 2-2-6. Schematic representation of internal reflection configuration for the two polarizations of interest. Note that all the components of the fields on the vacuum side of the interface are evanescent waves.[17]

The distance at which the amplitude of the electric field is $1/e$ is called the penetration depth d_p, given by the following equation:[19]

$$d_p = \frac{\lambda_2}{2\pi\sqrt{{n_1}^2 \sin^2\theta - {n_2}^2}}$$

where λ is the wavelength of the incident beam, θ is the angle of incidence, n_1 is the refractive index of a prism and n_2 is a refractive index of the sample (or vacuum). The

penetration depth is roughly 1/10 of the wavelength of the electric field, which is typically ca. 1 μm in the case of infrared spectroscopy.

2-2-4 *In Situ* IR Spectroelectrochemistry

There are several techniques of *in situ* IR spectroelectrochemistry to enhance its interfacial sensitivity including subtractively normalized interfacial Fourier transform IR spectroscopy (SNIFTIRS),[20,21] polarization modulation reflection-absorption spectroscopy (PM-IRRAS),[22,23] and surface-enhanced IR absorption spectroscopy (SEIRAS).[24,25] Osawa *et al.* demonstrated the advantage of SEIRAS by *in situ* and real-time monitoring of the redox reactions of heptylviologen (HV^{2+}) at a silver electrode as a model system.[26] The complicated voltammetric behavior of HV^{2+} was clearly observed in *in situ* IR spectra owing to the high sensitivity of SEIRAS (Figure 2-2-7).

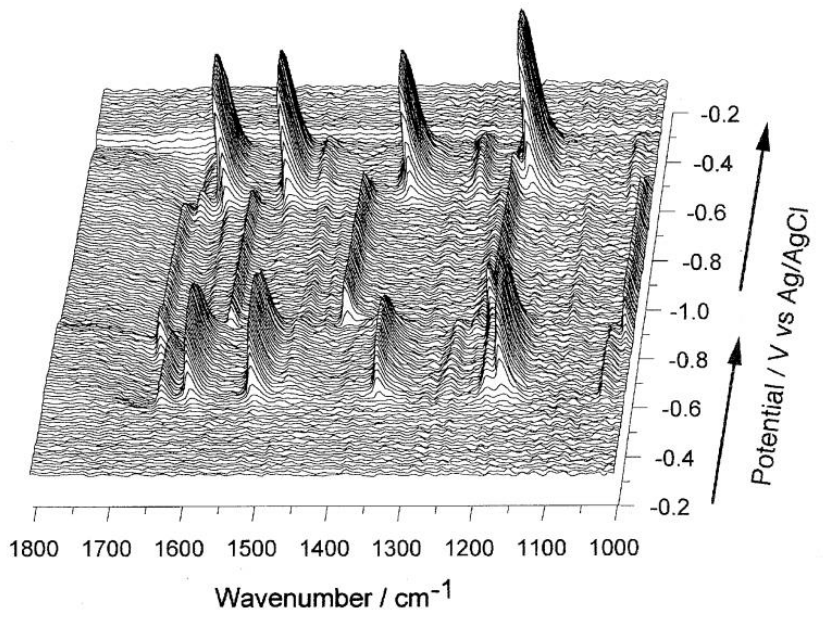

Figure 2-2-7. A series of IR spectra for the HV^{2+} reduction at a silver electrode collected simultaneously with the cyclic voltammogram. Each spectrum was collected with a 0.6 s acquisition time.[26]

These techniques are very effective for probing electrochemical dynamics at the electrode/electrolyte interface; however, they require specialized electrochemical system and a high degree of expertise. For example, SEIRAS technique requires a thin metal film substrate with island structure as a working electrode and SNIFTIRS technique can be used only for reversible systems.[24] In other words, these methods are not applicable to graphite electrodes and irreversible reactions. Therefore, in this dissertation, polarized ATR-IR configuration[27] was employed because it is a simple and enough setup to probe the irreversible redox reaction of TOT on the graphite electrode surface under an electrochemical condition.

2-2-5 Assignments Using Density Functional Theory Calculations

Density functional theory (DFT) is a computational quantum mechanical modelling method to simulate the electronic structure of atoms, molecules, and crystals. The calculation of a wide range of molecular properties using DFT allows comparison of theory and experiment and provides insight about the geometric, electronic, and spectroscopic properties of the systems.[28,29] Modern DFT rests on two theorems by Hohenberg and Kohn[30] and the Kohn-Sham (KS) approach.[31,32] Currently, mixed functionals such as B3LYP are in common use for vibrational analysis because better agreement between the calculated and experimental geometries, frequencies, and intensities is expected than the other types of density functionals.[33,34]

The assignment of the IR bands in the *in situ* IR spectrochemistry can be achieved by comparison with the theoretical spectra calculated by DFT and the IR spectra of the as-synthesized molecules. Vizintin *et al.* reported that the redox reaction mechanism of a poly(phenanthrene quinone)/reduced graphene composite (PFQ/rGO) cathode in a Li-

ion battery cell using operando IR ATR spectroscopy.[35] In the literature, DFT calculations were applied for assignments of the vibrations of FQ_3 and $LiFQ_3$ trimers (Figure 2-2-8(a)). The subtracted DFT spectra and subtracted spectra for the chemically synthesized reference monomers FQ and LiFQ (Figure 2-2-8(b)), which were very similar to the operando IR ATR spectra (Figure 2-2-8 (c)). In this dissertation, DFT calculations were employed for optimizing the geometry of a TOT single molecule and predicting its vibrational frequency to support the experimental IR spectra.

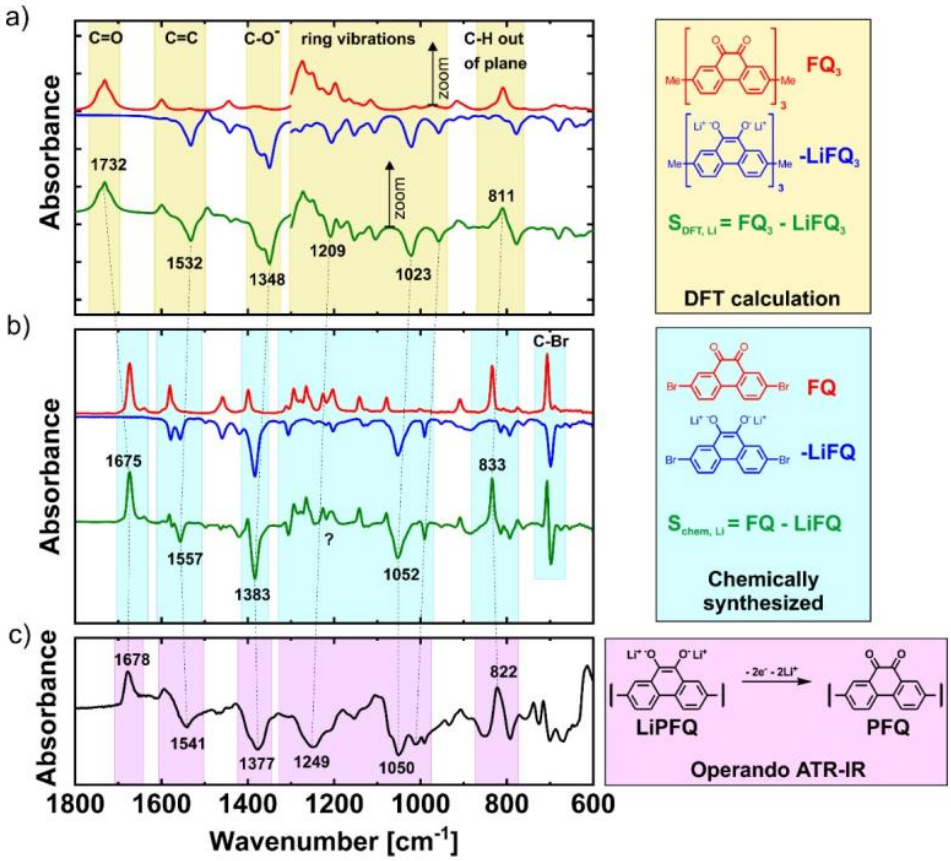

Figure 2-2-8. Comparison of (a) DFT calculation of model trimer, (b) measured IR spectra of chemically synthesized reference monomer and (c) operando ATR-IR spectra of Li-PFQ/rGO battery at the end of charge at 3.5 V vs. Li/Li+.[35]

2-3 Electron Microscopy

2-3-1 Types of Electron Microscopy

Electron microscopy enables imaging of nanoscale materials and characterization of their unique properties due to high resolution, wide magnification range, and electron generated signals. Scanning electron microscopy (SEM) are used to examine material surfaces by scanning sequentially across the sample with an incident of focused electron beam (Figure 2-3-1 (a)). Transmission electron microscopy (TEM) are used to examine the internal structure of samples by transmitted electrons in a defined area of the sample with an incident of spread electron beam. Scanning transmission electron microscopy (STEM) are hybrid of SEM and TEM, which detect transmitted electrons while scanning across the thin sample.

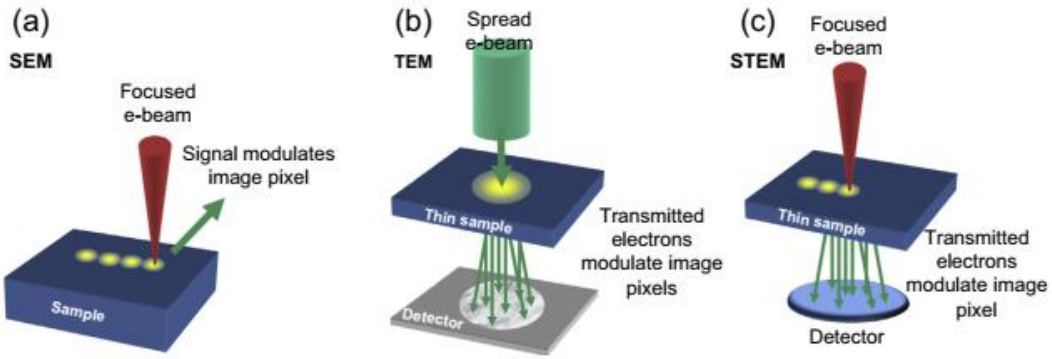

Figure 2-3-1. Schematic of SEM, TEM, and STEM imaging methodology. (a) Serial collection of data points in SEM. (b) Parallel image acquisition in TEM. (c) Serial collection of transmitted electrons in STEM.[36]

When a beam of electrons incidents on a sample, various types of signals are produced including secondary electrons (SE), backscattered electrons (BSE), characteristic X-rays and cathodoluminescence (CL) by interactions of the electron

beam with atoms at various depths within the sample. These signals can be detected and processed to perform microstructural imaging and structural or chemical characterization of specific areas of the sample.

2-3-2 Scanning Electron Microscopy (SEM)

SEM is used for imaging and analysis of sample surfaces. The typical components of an SEM microscope include the electron gun (electron source and accelerating anode), electromagnetic lenses to focus the electrons, a vacuum chamber housing the sample stage, and a selection of detectors to collect the signals emitted from the sample (Figure 2-3-2). SE imaging mode is usually used to image sample shape because SEs are abundant. In this dissertation, SEM was employed to observe the TOT neutral radical crystals electrodeposited on the graphite electrode surface by extracted from the electrochemical cell after the voltammetric measurements.

The electron source is one of the most important components in SEM. In standard microscopes, electrons are usually generated by heating a tungsten filament or a crystal of lanthanum hexaboride (LaB_6).[37] The tungsten filament is the most common types of electron source mainly due to its low price point, high reliability, and suitability for low magnification imaging. The LaB_6 crystal possess higher brightness output and longer life hours than the tungsten filament due to its lower work function. On the other hand, in a field emission SEM (FE-SEM), which has higher magnification and better resolution than SEM, no heating but a so-called “cold” source is employed.[38] The field emission gun features a single tungsten filament with an extremely thin and sharp tungsten needle (tip diameter 10 – 100 nm) works as a cathode which produces the emission of electrons caused by a strong electric field.

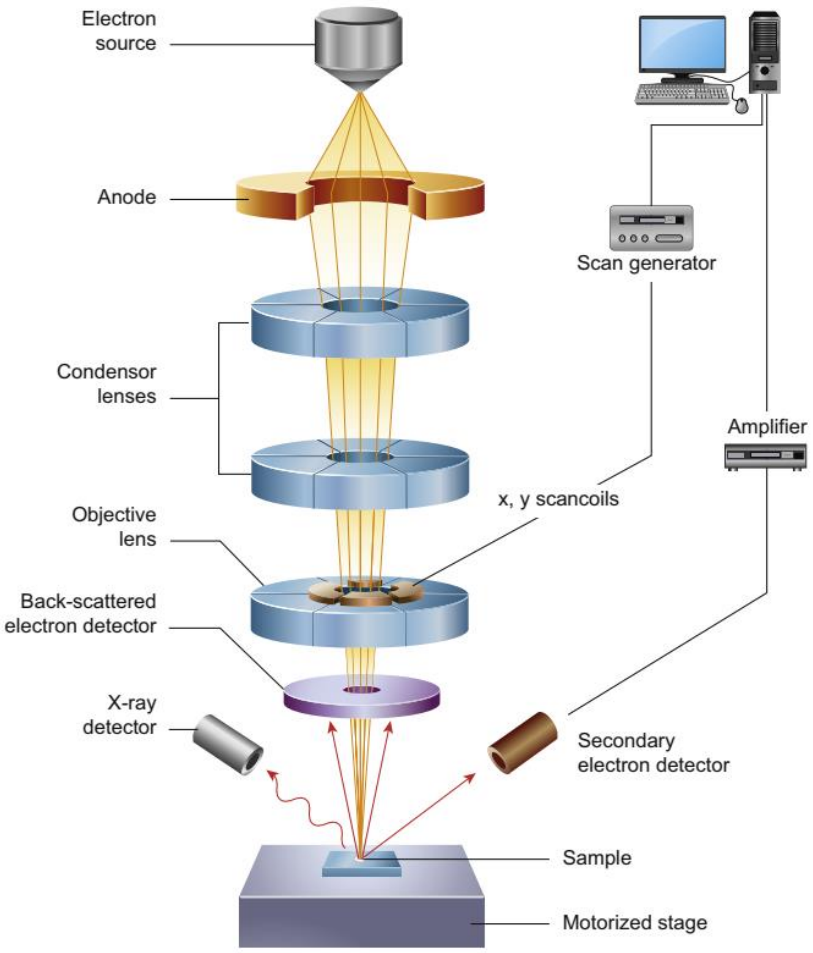

Figure 2-3-2. Schematic diagram of the core components of an SEM microscope.[36]

2-3-3 Scanning Transmission Electron Microscopy (STEM)

STEM is used for the analysis of sample internal microstructures, evaluation of nanostructures and imaging of atoms by using TEM microscopes. The typical components of a TEM microscope include the electron gun, electrostatic lenses, and a transmitted electron detection system (Figure 2-3-3). In the STEM mode, transmitted electrons are detected with axial bright-field (BF) for unscattered electrons and annular dark-field (ADF) and high angle ADF (HAADF) detectors for scattered electrons. HAADF images show very strong contrast modulations due to local changes in atomic

number of the sample reflecting composition at nanoscale. When a crystal is aligned in a favorable orientation with respect to the incident electron beam, elastically scattered electrons focused by the post-sample lenses form an electron diffraction pattern in the back focal plane of the objective lens. The crystallography of the sample can be determined by detailed analysis of this diffraction pattern.

Sample preparation for a TEM/STEM analysis is an important job. Focused ion beam (FIB) milling is one of the most popular preparation methods for TEM/STEM samples which may need to be 100 nm or thinner to transmit electrons. Dual beam FIB-SEM microscopes in particular have become very popular because they allow both high-resolution imaging and micromachining flexibility in a single instrument.[39] The electron transparent part of the sample prepared in FIB-SEM microscopes is usually ~ 5 μm × 20 μm (Figure 2-3-4).[40] In this dissertation, HAADF-STEM imaging and electron diffraction analysis were employed for the crystallographic characterization of a TOT crystal on the graphite electrode surface, while the sample was prepared from the post-reaction electrodes by FIB-SEM.

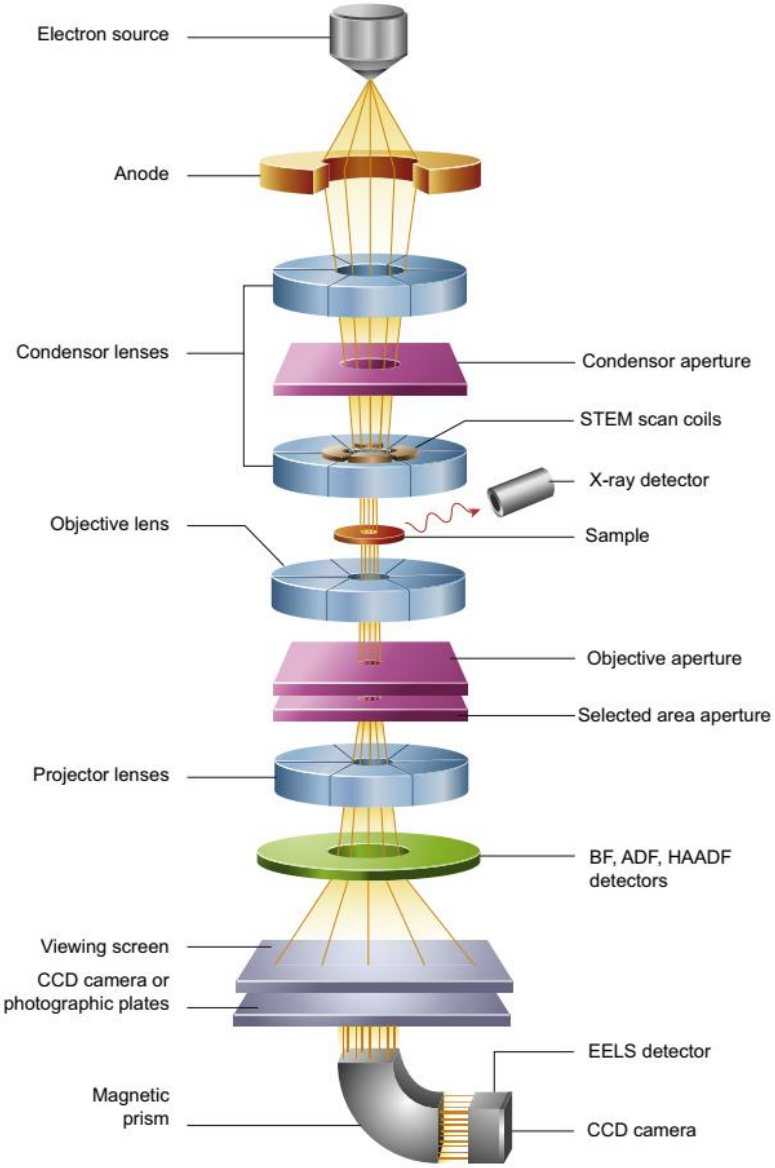

Figure 2-3-3. Schematic of core components of a TEM microscope.[36]

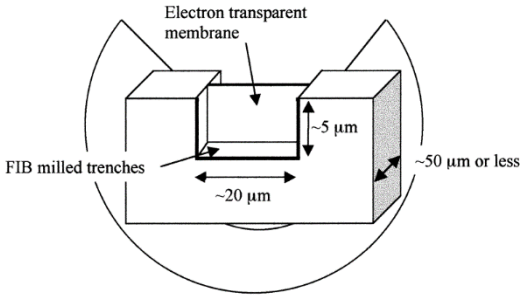

Figure 2-3-4. A schematic diagram of a prepared sample by FIB milling.[40]

References

1. N. Elgrishi, K. J. Rountree, B. D. McCarthy, E. S. Rountree, T. T. Eisenhart, J. L. Dempsey, *J. Chem. Educ.* **2018**, *95*, 197.
2. O. A. Farghaly, R. S. Abdel Hameed, A. A. H. Abu-Nawwas, *Int. J. Electrochem. Sci.* **2014**, *9*, 3287.
3. T. M. Nahir, R. A. Clark, E. F. Bowden, *Anal. Chem.* **1994**, *66*, 2595.
4. J. F. Rusling, S. L. Suib, *Adv. Mater.* **1994**, *6*, 922.
5. J. Heinze, *Angew. Chemie Int. Ed. English* **1984**, *23*, 831.
6. G. A. Mabbott, *J. Chem. Educ.* **1983**, *60*, 697.
7. A. J. Bard, L. R. Faulkner, *Electrochemical Methods : Fundamentals and Applications*, **2001**.
8. L. Cao, S. Sadaf, S. M. Beladi-mousavi, L. Walder, *Eur. Polym. J.* **2013**, *49*, 1923.
9. T. Suga, H. Ohshiro, S. Ugita, K. Oyaizu, H. Nishide, *Adv. Mater.* **2009**, *21*, 1627.
10. I. Lavagnini, R. Antiochia, F. Magno, *Electroanalysis* **2004**, *16*, 505.
11. J. Rupar, M. M. Aleksić, K. Nikolić, M. R. Popović-Nikolić, *Electrochim. Acta* **2018**, *271*, 220.
12. Y. Morita, T. Murata, A. Ueda, C. Yamada, Y. Kanzaki, D. Shiomi, K. Sato, T. Takui, *Bull. Chem. Soc. Jpn.* **2018**, *91*, 922.
13. C. Berthomieu, R. Hienerwadel, *Photosynth. Res.* **2009**, *101*, 157.
14. J. L. R. Arrondo, A. Muga, J. Castresana, F. M. Goñi, *Prog. Biophys. Mol. Biol.* **1993**, *59*, 23.
15. K. Kanai, T. Ikame, Y. Ouchi, K. Seki, *J. Appl. Phys.* **2009**, *105*, 023703.

16. K. Arihara, F. Kitamura, K. Nukanobu, T. Ohsaka, K. Tokuda, *J. Electroanal. Chem.* **1999**, *473*, 138.

17. Y. J. Chabal, *Surf. Sci. Rep.* **1988**, *8*, 211.

18. J. Umemura, S. Takeda, T. Hasegawa, T. Kamata, T. Takenaka, *Spectrochim. Acta Part A Mol. Spectrosc.* **1994**, *50*, 1563.

19. J. M. Andanson, A. Baiker, *Chem. Soc. Rev.* **2010**, *39*, 4571.

20. S. N. Port, D. J. Schiffrin, T. Solomon, *Langmuir* **1995**, *11*, 4577.

21. J. Zhang, F. C. Anson, *J. Electroanal. Chem.* **1992**, *331*, 945.

22. L. Vieira, R. Schennach, B. Gollas, *Phys. Chem. Chem. Phys.* **2015**, *17*, 12870.

23. M. Bieri, T. Bürgi, *J. Phys. Chem. B* **2005**, *109*, 22476.

24. M. Osawa, *Bull. Chem. Soc. Jpn.* **1997**, *70*, 2861.

25. K. I. Ataka, T. Yotsuyanagi, M. Osawa, *J. Phys. Chem.* **1996**, *100*, 10664.

26. M. Osawa, K. Yoshii, *Appl. Spectrosc.* **1997**, *51*, 512.

27. A. Davantès, G. Lefèvre, *Surf. Sci.* **2016**, *653*, 88.

28. M. Orio, D. A. Pantazis, F. Neese, *Photosynth. Res.* **2009**, *102*, 443.

29. F. Neese, *Coord. Chem. Rev.* **2009**, *253*, 526.

30. P. Hohenberg, W. Kohn, *Phys. Rev.* **1964**, *136*, B864.

31. W. Kohn, L. J. Sham, *Phys. Rev.* **1965**, *137*, A1697.

32. W. Kohn, L. J. Sham, *Phys. Rev.* **1965**, *140*, A1133.

33. A. A. El-Azhary, H. U. Suter, *J. Phys. Chem.* **1996**, *100*, 15056.

34. M. W. Wong, *Chem. Phys. Lett.* **1996**, *256*, 391.

35. A. Vizintin, J. Bitenc, A. Kopač Lautar, J. Grdadolnik, A. Randon Vitanova, K. Pirnat, *ChemSusChem* **2020**, *13*, 2328.

36. B. J. Inkson, *Scanning Electron Microscopy (SEM) and Transmission Electron Microscopy (TEM) for Materials Characterization*, Elsevier Ltd, **2016**.

37. M. Abd Mutalib, M. A. Rahman, M. H. D. Othman, A. F. Ismail, J. Jaafar, *Scanning Electron Microscopy (SEM) and Energy-Dispersive X-Ray (EDX) Spectroscopy*, Elsevier B.V., **2017**.

38. H. Yao, K. Kimura, *Mod. Res. Educ. Top. Microsc.* **2007**, 568.

39. T. L. Burnett, R. Kelley, B. Winiarski, L. Contreras, M. Daly, A. Gholinia, M. G. Burke, P. J. Withers, *Ultramicroscopy* **2016**, *161*, 119.

40. L. A. Giannuzzi, F. A. Stevie, *Micron* **1999**, *30*, 197.

Chapter 3

Electrochemical Behaviors and Structural Changes During the Redox Processes of Trioxotriangulene on Graphite Electrode Surfaces

3-1 Introduction

A cathode of LIB cells usually contains active materials, conductive additives, and binders. Because most organic cathode active materials possess low electronic conductivity, conductive additives are added to enhance the electronic conductivity of the cathode. As conductive additives, several types of carbon materials are usually employed including an acetylene black (AB),[1–3] a Ketjen black,[4,5] and a carbon nanotube (CNT).[6–8] Therefore, in the redox reaction of cathode active materials, it is important to understand the behavior of electron transfer not only at the active material/electrolyte interface but also at the active material/carbon material interface.

Lee *et al.* reported the CNT nanohybrid electrodes in which flavin molecules are non-covalently tethered on the surface of single-walled CNTs via π-π interaction exhibited a high specific energy density, cycle stability, and rate performance.[6] However, the loading content of flavin molecules was only between 40-50% in the hybrid composite. Ito *et al.* successfully demonstrated that TOT-based buckypaper (thin sheets made from an aggregate of CNT) cathodes including up to 90 wt% TOT neutral radical exhibited a high capacity and energy density in a coin-type cell. It should be noted that the rate and cycle performance of the buckypaper cathodes were dependent on loading content of TOT; the buckypaper containing 90 wt% of TOT showed lower rate and cycle performance than that containing 40 wt% of TOT. They discussed that the difference in charge/discharge behavior might be caused by difference in the adsorption and crystalline states of TOT in the CNT matrix. However, the mechanisms on the redox processes of TOT molecules on the surface of carbon materials are not fully understood.

In this chapter, we investigated electrochemical behaviors and structural changes during the redox processes of TOT on graphite electrode surfaces via voltammetry and

electron microscopy. CV measurements of TOT monoanion solution on the graphite electrode revealed the irreversible redox process. Electron microscopy analyzes of the post-reaction electrode suggested an orientation-dependent redox activity. A primitive schematic of redox mechanism was proposed from the results of voltammetry and electron microscopy.

3-2 Materials and Methods

3-2-1 Materials

TOT neutral radicals and Li salts of TOT monoanions (LiTOT) were synthesized as previously reported,[9–12] which were provided through the courtesy of Professor Yasushi Morita (Aichi Institute of Technology). Tetrabutylammonium perchlorate (TBAP), *N,N*-dimethylformamide (DMF), and ferrocene (98%) were purchased from Sigma-Aldrich (St. Louis, MO, USA) and used without further purification. An electrolyte solution of DMF containing 0.1 M TBAP as a supporting electrolyte and a sample solution of 25 mM LiTOT in the electrolyte solution were prepared. A solution of 1 mM ferrocene was prepared in the electrolyte and used as an external standard for the electrochemical system. Highly oriented pyrolytic graphite (HOPG, SPI-2 grade) was procured from ALLIANCE Biosystems (Osaka, Japan) and fleshly cleaved using adhesion tape just before electrochemical measurements. Graphite sheets (GRAPHINITY^{TM}) were provided by the Kaneka Corporation (Osaka, Japan) and used without any pretreatment.

3-2-2 Voltammetry

The custom-designed electrochemical cell was made of Teflon vessel equipped with a three-electrode system (Figure 3-2-1(a)). A basal plane of HOPG substrate or a graphite sheet was employed as a working electrode (WE). The effective area of the working electrode, as defined by the size of O-ring (P-6, perfluoro), was 0.28 cm^2. A platinum wire (0.7 mm in a diameter) and a platinum mesh (80 mesh) were employed as a reference electrode (RE) and a counter electrode (CE), respectively. The platinum wire was pretreated by flame-annealing with a butane burner and quenching in ultrapure water three times over. The cell was assembled and put in a desiccator under atmospheric pressure (Figure 3-2-1(b)). A Hokuto Denko HZ-5000 potentiostat (Tokyo, Japan) (Figure 3-2-1(c)) was connected to the cell though the electrodes equipped with the desiccator by using lead-wires with alligator clips. For the voltammetric measurements of TOT, with only the electrolyte solution in the cell, the electrode potential was fixed at the initial potential (−0.2 V vs. Pt) before starting the potential sweep. The sample solution was then added to the cell to obtain the desired concentration of TOT and stirred adequately under a nitrogen gas flow. After the mixed solution was left to rest, a potential sweep was initiated.

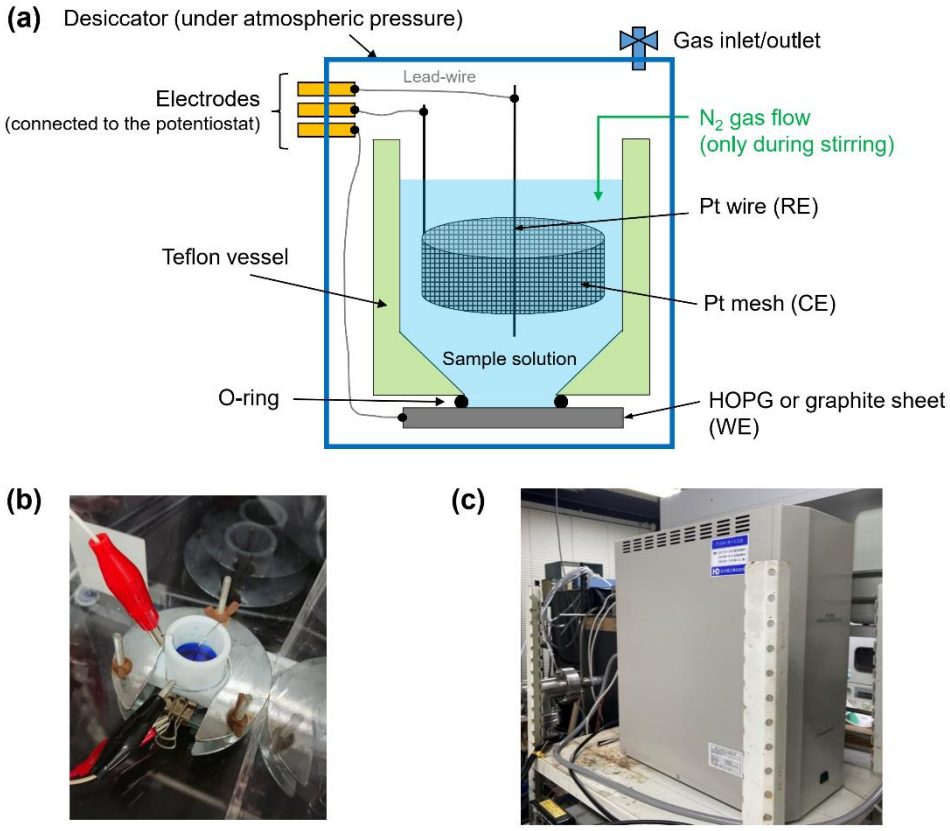

Figure 3-2-1. (a) Schematic of the electrochemical cell for the voltammeric measurements. (b, c) Photographs of the electrochemical cell and the potentiostat (HZ-5000, Hokuto Denko), respectively.

3-2-3 Electron Microscopy

A SEM microscope (JSM-IT100, JEOL) were used to observe the morphology of the post-reaction graphite electrodes. Before the SEM observations, the electrodes were dried under an ambient atmosphere at room temperature without any rinsing. Electron diffraction patterns were acquired using a Hitachi High-Tech HD-2700 TEM/STEM microscope (Tokyo, Japan) at an acceleration voltage of 200 kV and a stage temperature of −80 °C. The cross-sectional samples for the STEM analysis were prepared via lift-out using a FIB-SEM (Zeiss Crossbeam 550, Oberkochen, Germany) at an acceleration

voltage of 30 kV. The electron diffraction patterns were analyzed using the crystallographic software *Recipro*.[13] The sample preparation using FIB-SEM microscope, the TEM/STEM microscope operation, and the electron diffraction analysis were performed at Kaneka Techno Research Corporation.

3-3 Results and Discussion

3-3-1 CV Measurements

First, to confirm the electrochemical reaction between a monoanion and a neutral radical, CV measurements of TOT on the graphite sheet electrode were performed in the electrolyte solution containing the TOT monoanion. TOT in the neutral radical state is hardly soluble in the electrolyte solution as well as in typical organic solvents, whereas that in the monoanion state shows much higher solubility. Here, the graphite sheet was used as the WE. Graphite sheets are flexible and large-area films which are produced from graphitization of polyimide films by heat treatment above 3000°C, and their surface is regarded as a basal plane of graphite because their structure is a stack of highly oriented hexagonal carbon layers.[14,15] Regardless of 1 or 10 mM solutions, the CV curves of the graphite sheet electrodes (Figure 3-3-1(a) and (b)) were quite similar to those of the HOPG electrodes (Figure 3-3-1(c) and (d)). Therefore, we used the graphite sheet as the WE in this series of experiments because of the ease of following SEM, STEM, and IR measurements.

As shown in Figure 3-3-1(a), a couple of redox peaks was observed in the 1 mM solution at 0.41 and 0.25 V vs. Pt. The median of the peaks was calculated to be −0.07 V vs. Fc/Fc^+ using the redox potential of ferrocene as an external standard. These peaks can be attributed to the oxidation of monoanions and reduction of neutral radicals

because the potential value was comparable with previous results.[10] The peak widths and the separation of the redox peaks in the 10 mM solution (Figure 3-3-1(b)) were larger than those in the 1 mM solution (Figure 3-3-1(a)), suggesting that the reaction rates were not proportional to the concentration of TOT solutions.

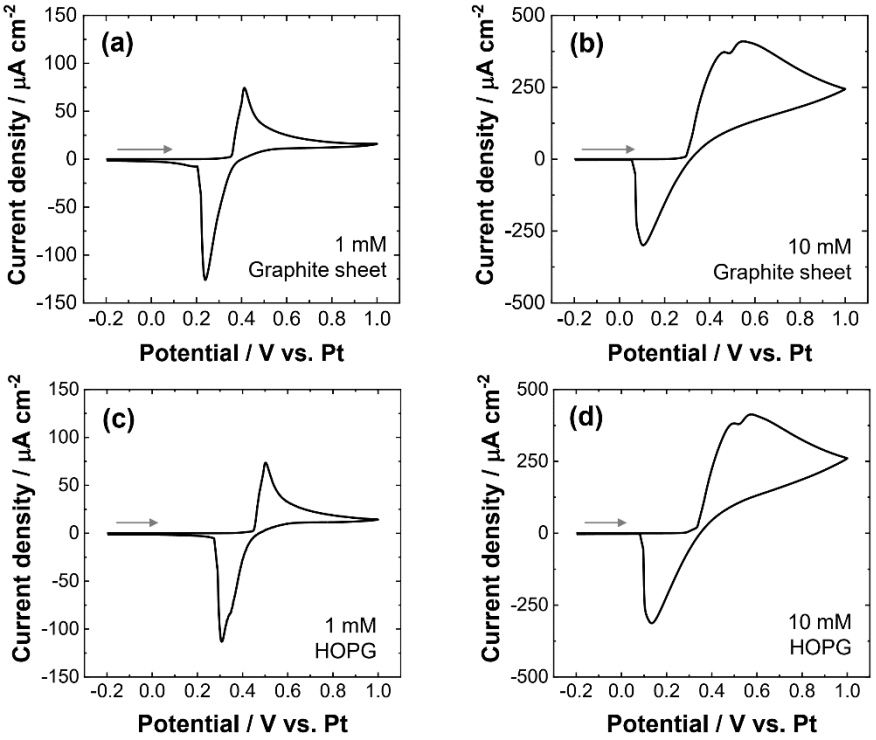

Figure 3-3-1. CV curves of TOT on the graphite electrodes in the (a, c) 1 mM, (b, d) 10 mM solutions for (a, b) the graphite sheet electrodes and (c, d) HOPG electrodes, respectively.

Multiple CV cycles of TOT on the graphite electrodes and the number of reacted molecules as a function of cycle number were shown in Figure 3-3-2. The number of reacted molecules was calculated from the integral of each peak area after the subtraction of the baseline by adopting Faraday's law as the reaction was regarded as a one-electron redox process. In the 1 mM solution, the anodic and cathodic peak were

diminished in the CV curves as the cycle was repeated (Figure 3-3-2(a)). At the first cycle, almost equal number of the molecules (26 and 24 nmol cm^{-2} for the oxidation and reduction, respectively) were involved in the redox processes, respectively. However, the number of reacted molecules decreased and the deviation between the oxidation and reduction increased as the cycle was repeated (Figure 3-3-2 (b)). This result suggests that the redox reaction occurred in a rather reversible manner at the first cycle but in an irreversible manner after the second cycle in the 1 mM solution. Meanwhile, in the 10 mM solution, even at the first cycle, deviation of the reacted molecules was large (327 and 107 nmol cm^{-2} for the oxidation and reduction, respectively). Peak diminishing in CV curves was observed as the cycle was repeated as in the case of the 1 mM solution (Figure 3-3-2(c)). The number of reacted molecules diminished but the deviation was approximately constant as the cycle was repeated (Figure 3-3-2(d)). This result suggests that the redox reaction occurred in an irreversible manner at any cycles in the 10 mM solution in the contrary to the 1 mM solution. Therefore, it was considered that the reversibility of the redox reaction depends on the concentration and the cycle number. The irreversible reaction may arise from the way of deposition of low-solubility neutral radical species. The reversibility, deposition, and dissolution of the neutral radical species on the electrode surface associated with oxidation and reduction should be further investigated.

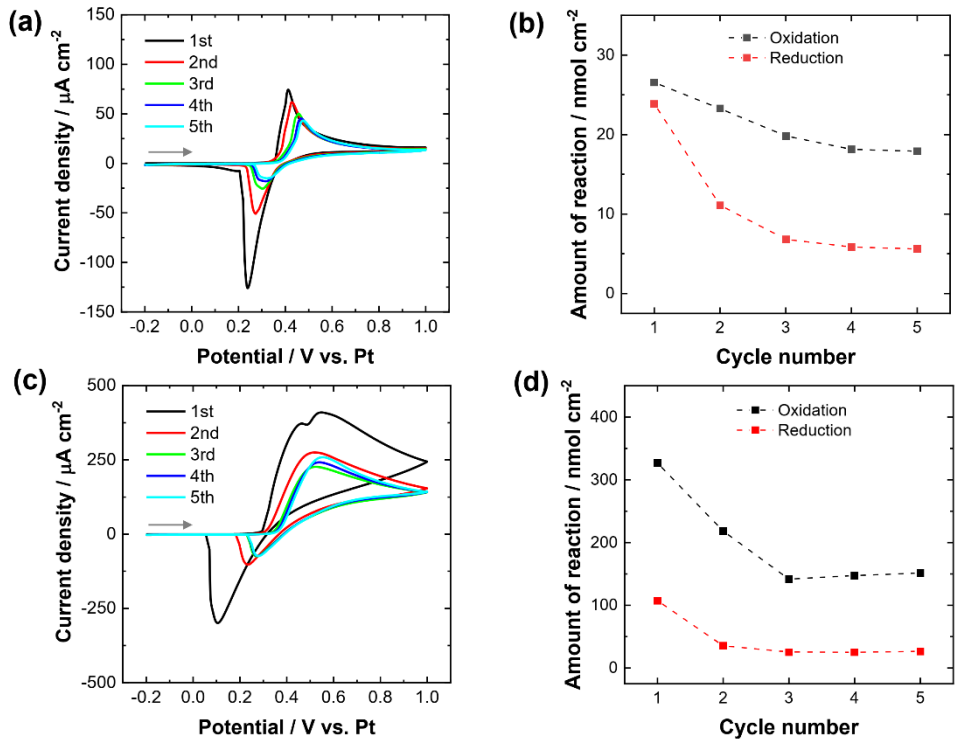

Figure 3-3-2. (a, c) Five CV cycles of TOT on the graphite electrodes and (b, d) the number of reactions calculated from the CV peaks as a function of cycle number in the (a, b) 1 mM and (c, d) 10 mM solutions.

3-3-2 SEM Observations

SEM observations of the post-reaction electrodes were performed to confirm the deposition and dissolution of TOT on the graphite electrode surface. Figure 3-3-3 shows the SEM images of the post-reaction electrodes at the first cycle quenched at the rising edge of the anodic peak (0.38 V in 1 mM; 0.4 V in 10 mM), the switching potential (1.0 V in 1 and 10 mM), and the end of the cycle (−0.2 V in 1 and 10 mM). In the 1 mM solution, columnar crystals of TOT neutral radicals were grown perpendicular to the electrode at 0.38 V (Figure 3-3-3(a)). As oxidation proceeded, the population and the length of the columnar crystals increased at 1.0 V (Figure 3-3-3(b)). In the reduction

process, almost all the columnar crystals disappeared at −0.2 V (Figure 3-3-3(c)). A similar behavior was observed in the second and third cycles (Figure 3-3-4). In contrast, in the 10 mM solution, the majority of the TOT crystals were grown perpendicular to the electrode, with the presence of some flat-lying crystals at 0.4 V (Figure 3-3-3(d)). As oxidation proceeded, the number of flat-lying crystals increased at 1.0 V (Figure 3-3-3(e)). During the reduction process, the upright crystals disappeared, whereas the flat-lying crystals remained (Figure 3-3-3(f)). These results suggest that the irreversibility of the CV measurements arises from the irreducibility of the flat-lying crystals, even at the cathodic potential.

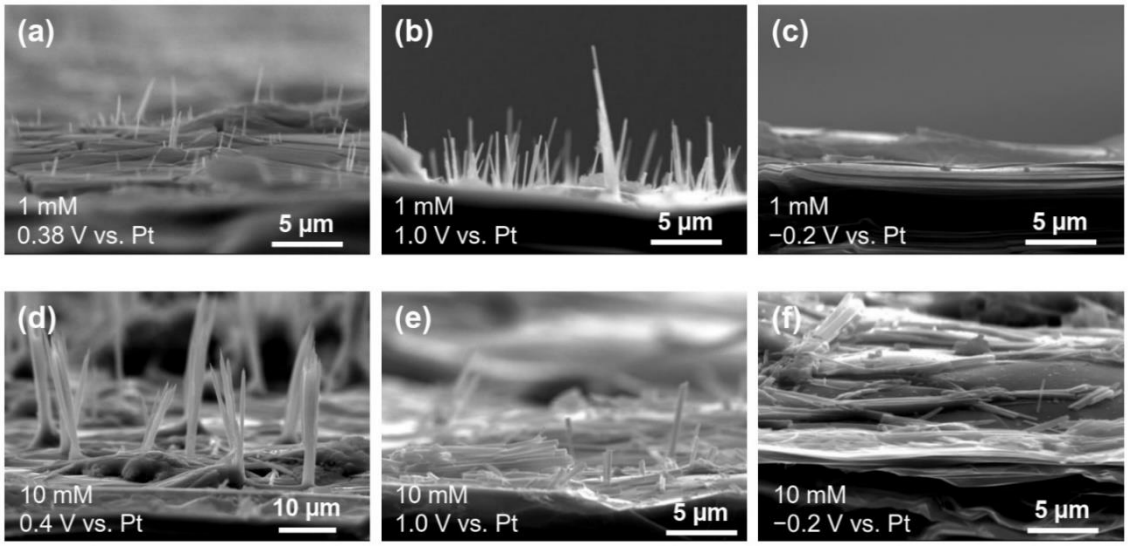

Figure 3-3-3. SEM images of the post-reaction electrodes quenched at different conditions: (a) 0.38, (b) 1.0, and (c) −0.2 V in the 1mM solution; (d) 0.4, (e) 1.0, and (f) −0.2 V in the 10 mM solution.

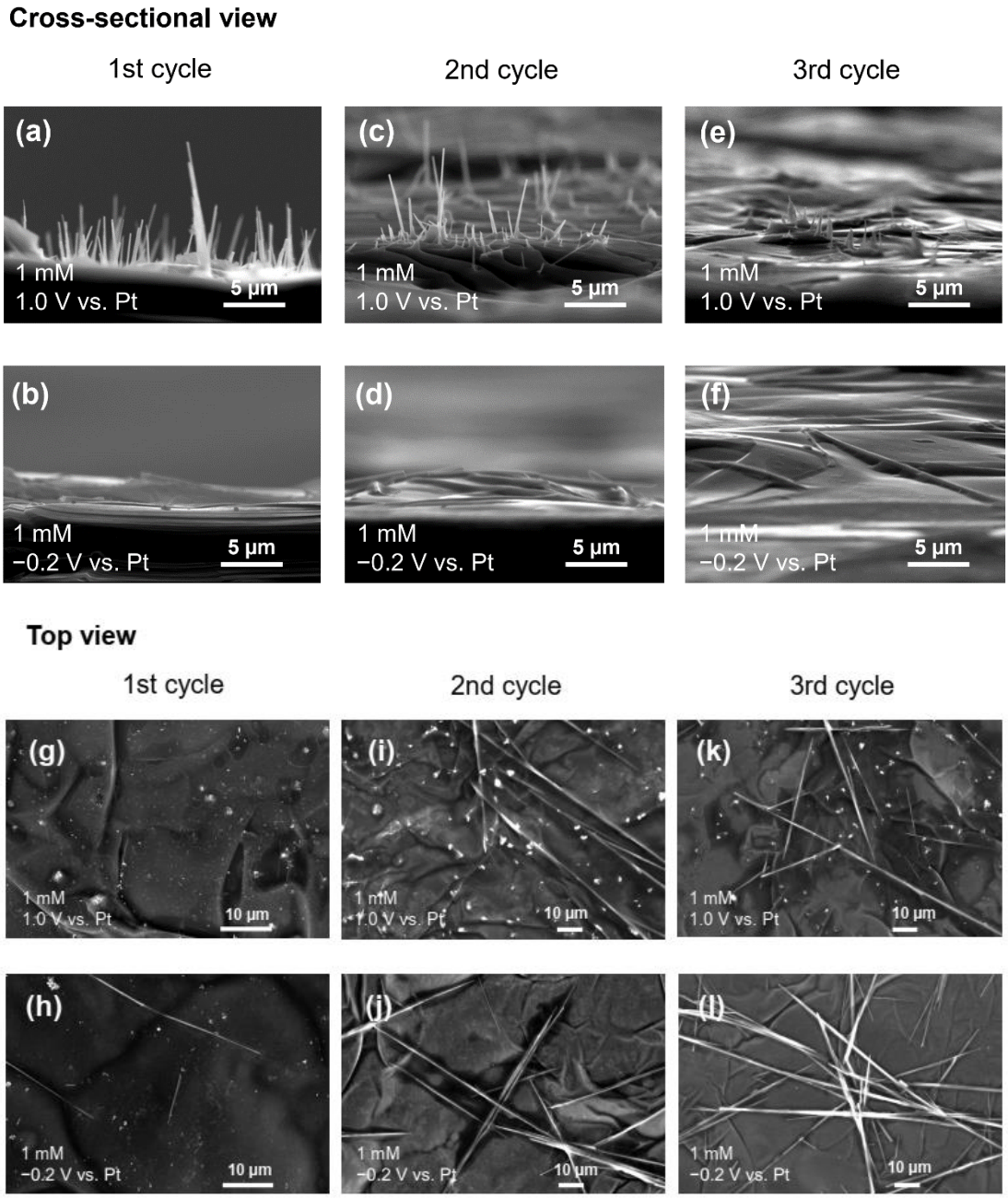

Figure 3-3-4. SEM images of the electrodes quenched at 1.0 V in the 1 mM solution: (a, g) first, (c, i) second, and (e, k) third cycles. SEM images of the electrodes quenched in the 1 mM solution at −0.2 V: (b, h) first, (d, j) second, and (f, l) third cycles. (a-f) Cross-sectional and (g-l) top views.

3-3-3 STEM Analysis

To characterize the columnar crystals on the graphite electrode, HAADF-STEM images (Figure 3-3-5(a)) and transmission electron diffraction patterns of the cross section of a crystal grown perpendicular to the electrode (Figure 3-3-5(b)) and the graphite electrode (Figure 3-3-5(c)) were acquired for the sample quenched at 1.0 V in the 10 mM solution. The columnar crystal was fixed to the electrode surface (Figure 3-3-5(a)), and the diffraction patterns in Figures 3-3-5(b) and (c) were consistent with the spots of a TOT neutral radical crystal in the <110> incidence[10] and graphite in the <120> incidence, respectively. Based on these results, the upright columnar crystal was confirmed to be a TOT neutral radical crystal with its *c*-axis perpendicular to the basal plane of the graphite.

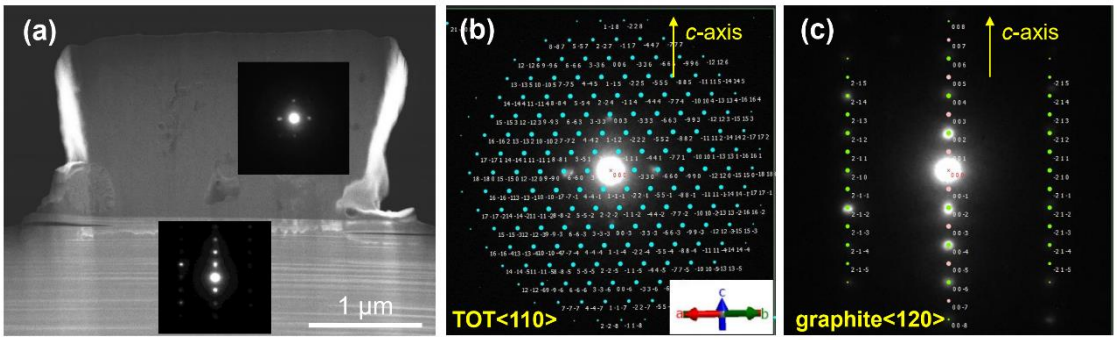

Figure 3-3-5. (a) HAADF-STEM image and transmission electron diffraction pattern of the cross section of a crystal grown perpendicular to the graphite electrode. Index mapping of the (b) crystal in the TOT <110> incidence and (c) graphite electrode in the graphite <120> incidence.

Figure 3-3-6 shows schematics of the orientation of TOT neutral radical crystals grown on the graphite electrode. Based on the SEM and STEM results, the TOT crystals grown perpendicular to the graphite electrode surface are regarded as having a face-on orientation (the π-plane of the TOT molecules is parallel to the basal plane of graphite). In contrast, the flat-lying crystals on the graphite electrode surface are regarded as having an edge-on orientation (the π-plane of the molecules is perpendicular to the basal plane). These results suggest that crystals with face-on orientation are reducible and dissolvable, whereas those with edge-on orientation are not.

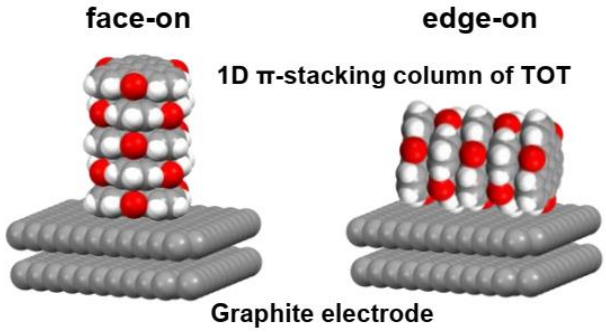

Figure 3-3-6. Schematics of the orientation of TOT neutral radical crystals grown on the graphite electrode.

3-4 Conclusions

The electrochemical behaviors and structural changes on the redox processes of TOT on the graphite electrode were investigated by voltammetry and electron microscopy. CV, SEM, and STEM analyses revealed that the growth/(partial) dissolution of columnar crystals of TOT neutral radicals occurred on the graphite during the oxidation/reduction of TOT monoanions in the electrolyte solutions. At a lower concentration (1 mM) of monoanions, upright columnar crystals (face-on orientation) were preferentially formed and dissolved in a rather reversible manner. At a higher

concentration (10 mM), more flat-lying columnar crystals (edge-on orientation) were formed, and such crystals remained on the graphite surface even at fully reduced potential owing to the lack of direct π-π interactions between the molecules and the graphite electrode. These results indicate that electron transfer characteristics between a TOT neutral radical crystal and a graphite surface are dependent on the molecular orientation.

References

1. M. Yao, S. I. Yamazaki, H. Senoh, T. Sakai, T. Kiyobayashi, *Mater. Sci. Eng. B Solid-State Mater. Adv. Technol.* **2012**, *177*, 483.
2. M. Kato, H. Sano, T. Kiyobayashi, N. Takeichi, M. Yao, *MRS Commun.* **2019**, *9*, 979.
3. X. Han, C. Chang, L. Yuan, T. Sun, J. Sun, *Adv. Mater.* **2007**, *19*, 1616.
4. H. Chen, M. Armand, M. Courty, M. Jiang, C. P. Grey, F. Dolhem, J. M. Tarascon, P. Poizot, *J. Am. Chem. Soc.* **2009**, *131*, 8984.
5. Z. Song, Y. Qian, X. Liu, T. Zhang, Y. Zhu, H. Yu, M. Otani, H. Zhou, *Energy Environ. Sci.* **2014**, *7*, 4077.
6. M. Lee, J. Hong, H. Kim, H. D. Lim, S. B. Cho, K. Kang, C. B. Park, *Adv. Mater.* **2014**, *26*, 2558.
7. H. Ito, T. Murata, M. Fujisaki, R. Tsuji, Y. Morita, *ChemSusChem* **2021**, *14*, 1377.
8. A. Aqil, A. Vlad, M. Piedboeuf, M. Aqil, N. Job, S. Melinte, C. Detrembleur, J. Christine, *Chem. Commun.* **2015**, *51*, 9301.

9. Y. Morita, S. Nishida, T. Murata, M. Moriguchi, A. Ueda, M. Satoh, K. Arifuku, K. Sato, T. Takui, *Nat. Mater.* **2011**, *10*, 947.

10. Y. Morita, T. Murata, A. Ueda, C. Yamada, Y. Kanzaki, D. Shiomi, K. Sato, T. Takui, *Bull. Chem. Soc. Jpn.* **2018**, *91*, 922.

11. H. Ito, T. Murata, T. Miyata, M. Morita, R. Tsuji, Y. Morita, *ACS Omega* **2019**, *4*, 17569.

12. T. Murata, S. Nakanishi, H. Nakayama, H. Ito, M. Morita, R. Tsuji, Y. Morita, *ACS Appl. Energy Mater.* **2022**, *5*, 1218.

13. Y. Seto, M. Ohtsuka, *J. Appl. Crystallogr.* **2022**, *55*, 397.

14. M. Murakami, K. Watanabe, S. Yoshimura, *Appl. Phys. Lett.* **1986**, *48*, 1594.

15. M. Murakami, A. Tatami, M. Tachibana, *Carbon* **2019**, *145*, 23.

Chapter 4

Mechanistic Investigations on the Redox Processes of Trioxotriangulene on the Graphite Electrode Surface by *In Situ* Infrared Spectroelectrochemistry

4-1 Introduction

In Chapter 3, a preliminary model on the electron transfer and the redox activity of TOT on the graphite surface was proposed. However, there are two problems on detailed mechanistic investigation. First, SEM observations are not applicable in the early stage of deposition formation because the resolution limitation of SEM prevents observation of nanometer-scale molecular aggregates. Second, the electrochemical dynamics on the graphite electrode surface are still unclear through the procedure that the electrode is quenched at a different potential, removed from the cell, and dried in ambient atmosphere.

In this chapter, to overcome these drawbacks, *in situ* IR spectroelectrochemisty was adopted for mechanistic investigations on the redox process of TOT on the graphite electrode surface. Prior to *in situ* IR measurements, IR characterization of TOT on the graphite electrodes was performed by IR ATR spectroscopy, DFT calculations, and IR RA spectroscopy. Consequently, *in situ* IR spectroelectrochemistry was performed. *In situ* IR spectroelectrochemical analyses successfully characterized the alignment of the columnar crystals of the TOT neutral radicals and their electrochemical behaviors, including the possible origins of the irreversible redox reaction of TOT on the graphite electrode.

4-2 Materials and Methods

4-2-1 Materials

TOT neutral radicals and LiTOT were synthesized as previously reported,[1–4] which were provided through the courtesy of Professor Yasushi Morita (Aichi Institute of

Technology). Tetrabutylammonium perchlorate (TBAP) and *N,N*-dimethylformamide (DMF) were purchased from Sigma-Aldrich (St. Louis, MO, USA) and used without further purification. An electrolyte solution of DMF containing 0.1 M TBAP as a supporting electrolyte and a sample solution of 25 mM LiTOT in the electrolyte solution were prepared. Graphite sheets (GRAPHINITY^{TM}) were provided by the Kaneka Corporation (Osaka, Japan) and used without any pretreatment. Acetylene black (AB) and polyvinylidene difluoride (PVDF) in *N*-methyl-2-pyrrolidone solution (KF polymer) were purchased from Denka (Tokyo, Japan) and Kureha (Tokyo, Japan), respectively, and were used to prepare a conductive adhesive by compounding AB and PVDF at a ratio of 7/3 w/w.

4-2-2 IR ATR Spectroscopy of Powder Samples

The IR ATR spectra of the powder samples were obtained using a Thermo Fisher Scientific Nicolet iS50 FT-IR spectrometer (Madison, WI, USA), which is commonly used for other *ex situ* IR spectroscopic measurements, equipped with an ATR attachment having an ATR prism of Ge. The angle of incidence was fixed at 45°. A liquid-N_2-cooled mercury cadmium telluride (MCT) detector was employed to detect IR light with a modulation frequency of 50 kHz. All spectra were recorded at a resolution of 1 cm^{-1}.

4-2-3 *Ex Situ* IR RA Spectroscopy

Ex situ IR RA spectral measurements were performed using a Spectra-Tech FT-80 specular reflectance accessory with a wire-grid polarizer (Oak Ridge, TN, USA) (Figure

4-2-1). The angles of incidence and polarization were set to 80° and 90°, respectively, generating p-polarization. The background spectrum measurement was performed on a pristine graphite sheet surface, which was used for sample measurements. In the *ex situ* IR RA measurement, the graphite sheet electrodes with the size of 27 × 27 mm^2 were employed because the diameter of the IR beam spot on the sample surface was ca. 20 mm. The measurement of IR ATR spectroscopy of powder samples (Section 4-2-2) and *ex situ* IR RA spectroscopy (Section 4-2-3) was performed at Kyoto University through the courtesy of Professor Takeshi Hasegawa (Kyoto University).

Figure 4-2-1. Photograph of the specular reflectance accessory (FT-80, Spectra-tech) with a wire-grid polarizer attached to a spectrometer.

4-2-4 *In Situ* ATR IR Spectroelectrochemistry

An *in situ* IR ATR spectroelectrochemical measurement cell was designed and constructed in cooperation with S.T. Japan, Inc. (Tokyo, Japan). A schematic of the cell setup is shown in Figure 4-2-2. The cell made of polyether-ether-ketone (PEEK) was equipped with a single-reflection ZnSe crystal, which functions as an ATR element,

attached to a PIKE Technologies VeeMAX III angle-variable specular reflection accessory (Madison, WI, USA) (Figure 4-2-2(a)). The angle of incidence was fixed at 45°. A graphite sheet with a diameter of 4 mm was used as the WE and positioned such that the signal from graphite could be detected. A micrometer screw was used to accurately control the distance between the WE and the ZnSe crystal. The graphite sheet was bonded to a stainless-steel plate using the AB/PVDF composites and a Pt mesh and wire were used as the CE and RE, respectively (Figure 4-2-2(c)). FT-IR spectra were recorded on a Bruker Vertex70 spectrometer (Billerica, MA, USA) equipped with a liquid-N_2-cooled MCT detector. The spectra were recorded with s-polarization of the incident IR beam using an IR-OPT02 wire grid polarizer (JEOL, Tokyo, Japan). All spectra were recorded at a resolution of 4 cm^{-1} with 1024 accumulations. Electrochemical measurements were performed using a Hokuto Denko HSV-110 mobile potentiostat system. All the measurements were performed at room temperature.

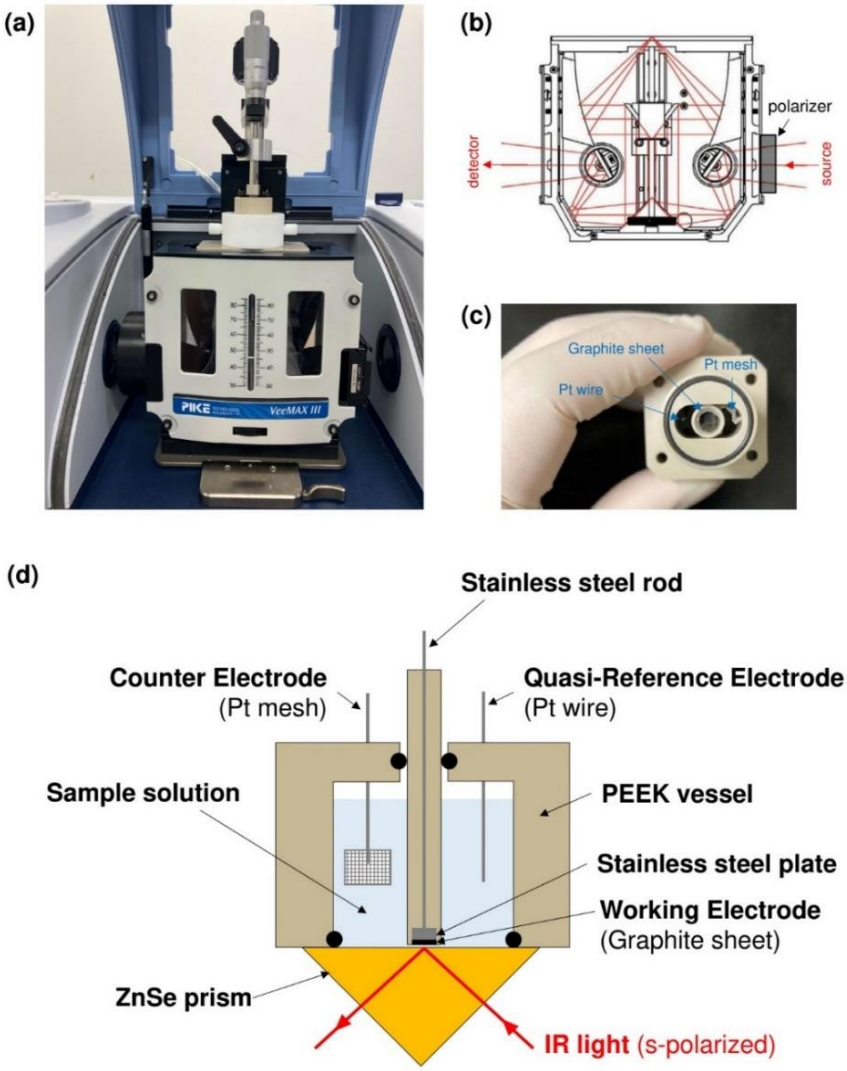

Figure 4-2-2. (a) A photograph of *in situ* IR ATR spectroelectrochemisry setup in this dissertation. (b) The optical path inside the angle-variable specular reflection accessory (VeeMAX III, PIKE Technologies). (c) A bottom view of the spectroelectrochemical cell. (d) A schematic image of the spectroelectrochemical cell.

4-2-5 SEM and Optical Microscopy

A JEOL S-4800 FE-SEM microscope and a KEYENCE VH-5500 digital microscope (Osaka, Japan) were used to observe the surface of the post-reaction graphite electrodes and the ATR prism, respectively. Before the FE-SEM and microscope observations, the electrodes and prisms were dried under an ambient atmosphere at room temperature without any rinsing.

4-2-6 DFT Calculations

DFT calculations were performed using Gaussian 09.[5] The B3LYP functional with the 6-31+G basis set was used to optimize the geometry of the TOT neutral radical and to calculate the vibrational frequencies and IR signals.

4-3 Results and Discussion

4-3-1 FT-IR Characterization of TOT Neutral Radical Species

Prior to the *in situ* IR measurements, *ex situ* IR RA spectra of the post-reaction graphite electrode quenched at different potentials were acquired to characterize the absorption bands and molecular orientations of the TOT neutral radical forming the columnar crystals. RA spectroscopy is a powerful technique used to analyze molecular orientation on a metallic substrate[6] involving HOPG[7] through the surface selection rule of RA spectrometry, in which only the surface-normal component of a transition moment is selectively observed.

First, the IR ATR spectrum of the as-synthesized TOT neutral radical powder was acquired (Figure 4-3-1(a)) to analyze the RA spectra. Based on the SEM and STEM

results, the RA spectra of the post-reaction electrodes quenched at 0.47 and −0.2 V (Figure 4-3-1(b)) correspond to the face-on and edge-on orientations, respectively. The changes in the RA spectra of these two samples support the different orientations of the TOT molecules. The prominent absorption peaks in the RA spectra were assigned by comparing the IR ATR spectrum of the TOT neutral radical powder (Figure 4-3-1(a)) with the simulated spectra of the TOT molecule obtained using DFT calculations (Table 4-3-1). The C–H out-of-plane bending modes (757, 789 and 860 cm^{-1}) and both in-plane ring-deformation mode (921 cm^{-1}) and in-plane ring-stretching modes (1334 and 1357 cm^{-1}) were selectively observed in the RA spectra of the post-reaction electrodes quenched at 0.47 and −0.2 V, respectively (Figure 4-3-1(b)). Considering the surface selection rule of RA spectrometry, these results indicate that the TOT molecules have face-on and edge-on orientations at 0.47 and −0.2 V, respectively, which is consistent with the SEM and STEM results.

Assignment of all the peaks is challenging because the peak position and intensity of the calculated spectra do not correlate well with the experimentally measured spectra. Nevertheless, the peaks mentioned above are useful as marker bands to discuss the molecular orientation of the molecules on the electrodes. These results suggest that the deposition/dissolution behavior and molecular orientation changes accompanied by redox reactions can be directly observed by *in situ* IR spectroelectrochemistry.

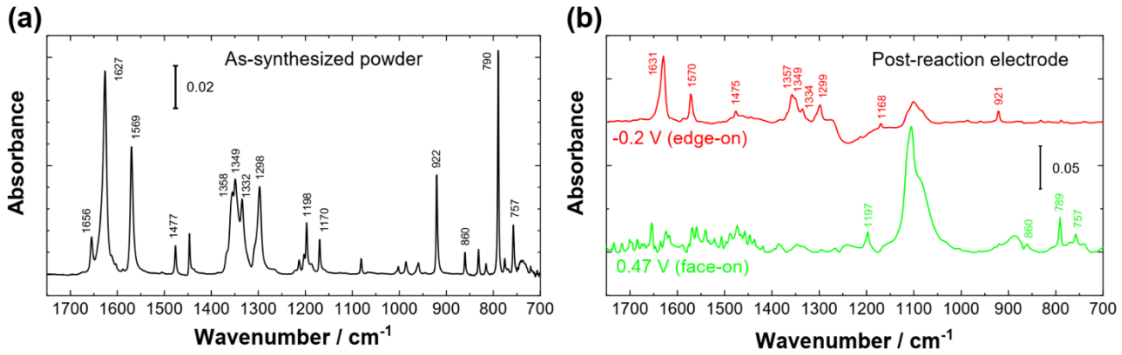

Figure 4-3-1. (a) IR ATR spectrum of the as-synthesized TOT neutral radical powder. (b) IR RA spectra of the post-reaction graphite electrodes quenched at 0.47 and −0.2 V.

Table 4-3-1. Absorption-peak assignment for the TOT neutral radical species in the IR ATR and RA spectra.

ATR (cm^{-1})	RAS (cm^{-1})		DFT calculation (cm^{-1})	Assignment	Vibrational direction against the molecular plane
	−0.2 V (edge-on)	0.47 V (face-on)			
757		757	763	γ (C-H)	out-of-plane
790		789	763	γ (C-H)	out-of-plane
860		860	878	γ (C-H)	out-of-plane
922	921		956	δ (ring)	in-plane
1170	1168				
1198		1197			
1298	1299				
1332	1334		1337	ν (ring)	in-plane
1358	1357		1374	ν (ring)	in-plane
1477	1475				
1569	1570		1581	ν (C=O) δ (C-H)	in-plane
1627	1631		1627	ν (ring) δ (C-H)	in-plane

4-3-2 *In Situ* IR ATR Spectroelectrochemistry

In situ IR ATR spectra were acquired using a chronoamperometric multistep sequence. The spectrum was recorded at the first potential step (−0.2 V vs. Pt) to measure the background. Considering the CV results (Figures 3-3-1 and 3-3-2), no Faradaic reactions should occur at this potential. All spectra recorded at different applied potentials were then normalized to this background. Thus, compared with the background spectrum, positive bands indicate an increase in absorbance, whereas negative bands indicate a decrease in absorbance. From −0.2 V, the potential was stepped in the anodic direction until 1.0 V and then back in the cathodic direction until −0.2 V. Note that only the surface-parallel components of a transition moment are selectively observed in these spectra because of the s-polarized ATR configuration employed, which is contrary to the RA spectra.

The absorbance spectra in the 1 and 10 mM solutions are shown in Figures 4-3-2(a) and 4-3-2(b), respectively. Only a slight spectral change was observed upon stepping the applied potential, as the signal intensities were very small. Hence, we calculated the second-derivative spectra to quantitatively evaluate the spectral changes. Derivative spectra can resolve or enhance smaller peaks that are apparently partially resolved from larger peaks due to background and/or are buried in the noise, and their intensities are found to be proportional to those of the original spectra.[8–11] The second-derivative spectra of the 1 and 10 mM solutions are shown in Figures 4-3-2(c) and 4-3-2(d), respectively. The positive/negative bands in the second-derivative spectra correspond to the negative/positive bands in the original absorbance spectra. Absorption bands derived from the TOT neutral radicals appeared at 758, 789, 860, and 920 cm^{-1}. The bands at 758 cm^{-1}, corresponding to the edge-on orientation (C–H out-of-plane bending modes),

and 920 cm^{-1}, corresponding to the face-on orientation (in-plane ring-deformation mode), were chosen as marker bands to elucidate the molecular orientations because they did not overlap with other absorption bands.

In the second-derivative spectra of the 1 mM solution (Figure 4-3-2(c)), upon stepping the potential positively from −0.2 to 0.35 V, no absorption corresponding to the TOT neutral radical was observed. By stepping from 0.4 to 1.0 V, an absorption band at 920 cm^{-1} appeared. Upon stepping back from 1.0 to −0.2 V, an absorption band at 758 cm^{-1} was observed in addition to the band at 920 cm^{-1}. Meanwhile, in the second-derivative spectra of the 10 mM solution (Figure 4-3-2(d)), upon stepping the potential from −0.2 to 0.25 V, no absorption corresponding to the TOT neutral radical was observed. By stepping positively from 0.4 to 1.0 V and negatively from 1.0 to −0.2 V, the absorption bands at 758 and 920 cm^{-1} were observed.

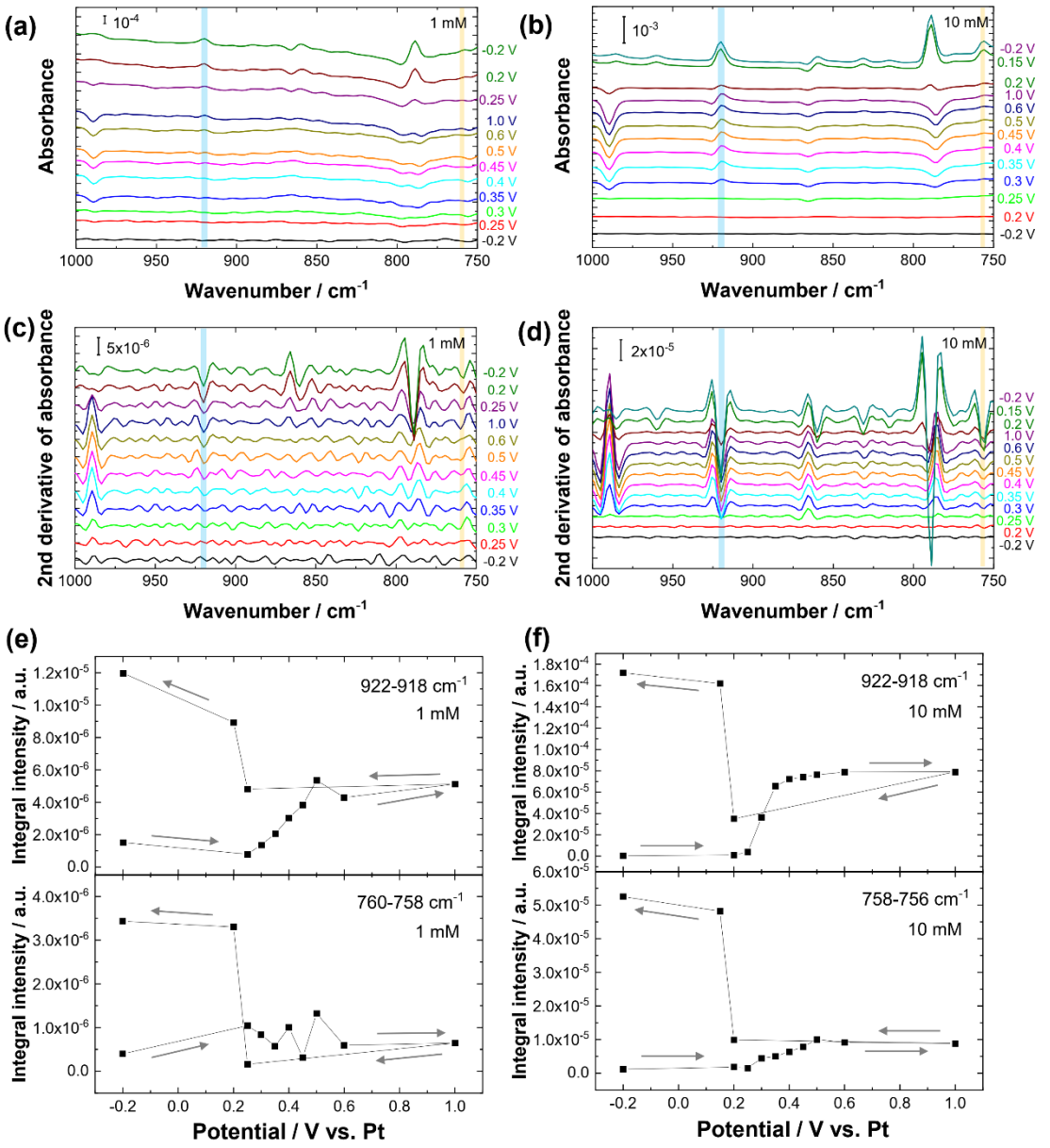

Figure 4-3-2. (a, b) *In situ* IR ATR spectra, (c, d) second-derivative spectra, and (e, f) integral intensity calculated from the second-derivative spectra as a function of electrode potentials (measured from the bottom to the top) in the (a, c, e) 1 mM and (b, d, f) 10 mM solutions.

To estimate the population of the face-on and edge-on orientations, integral intensities were calculated from the second-derivative spectra in the region of each band and plotted as a function of electrode potential (Figures 4-3-2(e) and 4-3-2(f)). In the 1 mM solution, upon stepping positively from 0.25 to 0.5 V, there was an increase in the absorption band at 920 cm^{-1}. From 0.5 to 1.0 V, there was a saturated increase in the absorption in this region. In contrast, the intensity of the absorption band at 758 cm^{-1} remained relatively the same from −0.2 to 1.0 V. These behaviors indicate that the deposition and crystal growth during the oxidation process occurred in the face-on orientation. On the contrary, stepping negatively from 1.0 to −0.2 V increased the intensities of both bands. This unexpected behavior was caused by the failure of the quantitative analysis, which will be discussed later. For the 10 mM solution, upon stepping positively from 0.2 to 1.0 V, there was a significant increase in the absorption bands at 920 and 758 cm^{-1}, which indicates that deposition and crystal growth occurred in the face-on and edge-on orientations simultaneously. Stepping negatively from 1.0 to 0.2 V decreased the intensity of the 920 cm^{-1} band; however, the intensity of the band at 758 cm^{-1} was maintained, which indicates that reduction and dissolution occurred only in the face-on orientation. The increase in the intensities of both bands in the potential range of 0.2 to −0.2 V is not discussed here due to the same reason as in the case of the 1 mM solution.

The post-reaction electrode and prism surfaces were observed using FE-SEM and optical microscopy (Figure 4-3-3). No crystalline deposit was observed on the 1 mM post-reaction electrode (Figure 4-3-3(a)), whereas columnar crystals of edge-on orientation were observed on the 10 mM post-reaction electrode (Figure 4-3-3(c)). Needle-like crystalline materials were observed on both post-reaction ATR prism

surfaces (Figures 4-3-3(b) and 4-3-3(d)). These results suggest that the upright columnar crystals (face-on orientation) could be dissolved by reduction; however, some of the crystal fragments were detached from the electrode and deposited randomly on the underlying ATR prism during the reduction process (see Figure 4-2-2 for the configuration of IR ATR), increasing the areas of the bands at 920 and 758 cm^{-1} (due to a higher IR intensity of the evanescent wave at the ATR prism surface) when stepping negatively from 0.2 to −0.2 V (Figures 4-3-2(e) and 4-3-2(f)). Thus, the quantitative IR analyses during the reduction process between 0.2 V and −0.2 V were hindered by the detached crystals deposited on the ATR prism surface.

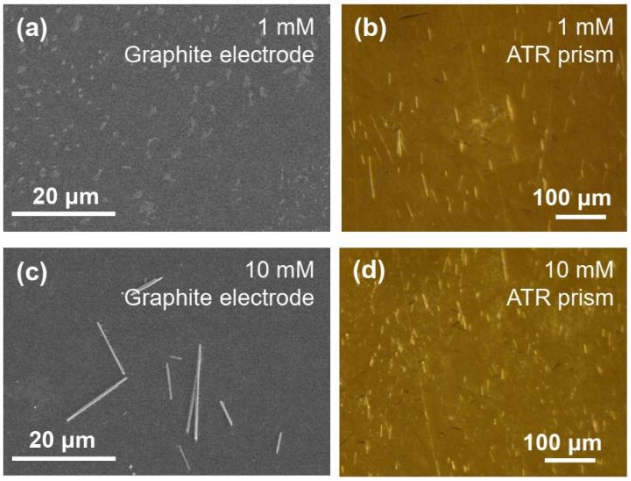

Figure 4-3-3. (a, c) FE-SEM images of the post-reaction electrode surfaces and (b, d) optical images of the post-reaction prism surfaces in the (a, b) 1 mM and (c, d) 10 mM solutions.

4-3-3 Mechanistic Model of TOT on the Graphite Electrode Surface

Figure 4-3-4 shows a schematic of the oxidation/reduction process of TOT on graphite electrodes, accompanied by deposition/dissolution. In the oxidation process of TOT monoanions in an electrolyte, the adsorption of oxidized TOT neutral radicals on graphite surfaces may be more stable in the face-on orientation than in the edge-on orientation owing to π–π interactions between the molecules and electrodes, and strong intermolecular interactions result in the growth of columnar crystals perpendicular to the electrode (1 mM).[3,4] Oxidation of a TOT monoanion at the top of the upright columnar crystal by electron conduction to the electrode through the π–π-stacked column can also be a possible growth route. Owing to the vigorous deposition at higher concentrations of TOT monoanions (10 mM), a higher collision rate of TOT neutral radicals on the electrode was observed, which may result in a higher rate of random nuclear formation of the stacked species, some of which can result in the formation of flat-lying crystals (edge-on orientation). The lack of efficient reduction for the flat-lying columnar crystals (remaining on the electrode surface even after applying a fully reducible potential) suggests that oxidation of the TOT monoanion at the edge of the flat-lying crystal does not occur; instead, a TOT neutral radical formed via oxidation on the electrode is incorporated in the flat-lying crystal.

In the reduction process of the columnar crystals of TOT neutral radicals on graphite, the flat-lying crystals (edge-on orientation) are inactive and remain on the surface because of the lack of direct π–π interactions between the molecules and the graphite electrode, as aforementioned. This indicates that electron transfer from graphite to the TOT neutral radical in flat-lying crystals is quite limited even when the crystal is aligned to the graphite electrode owing to the lack of π–π interactions between the edge-

on-lying molecule and the electrode surface. For upright columnar crystals, the reduction of a TOT neutral radical at the top of the crystal, via electron conduction from the electrode through the π–π-stacked column, should be much more efficient. It can explain the aforementioned result stating that rather reversible redox was observed in the 1 mM solution, where upright columnar crystals were preferentially formed.

Here, we should take note of how the needle-like crystal fragments were deposited on the ATR prism during the reduction process (Figure 4-3-3). Judging from the diameter and length (and the increase in the ATR signal (Figures 4-3-2(e) and 4-3-2(f)), the crystal fragments deposited on the ATR prism should be the columnar crystal fragments of TOT neutral radicals and mainly originated from the upright columnar crystal because the fragments were deposited in the reduction process at a potential range between 0.2 V and −0.2 V. The most probable explanation for the deposition of crystal fragments on the ATR prism placed at the bottom of the cell (Figure 4-2-2(d)) is the dissolution of a reduced TOT monoanion in the middle of the upright columnar crystals (face-on orientation) instead of the reduction of a TOT neutral radical at the top of the crystal. Once the fragments were detached from the electrodes, further reactions were inhibited. In the configuration of the CV analyses (Figure 3-2-1(a)), the same phenomenon occurred during the reduction, resulting in the deposition of some crystal fragments on the graphite electrode surface, which cannot be reduced at the electrode. The SEM images in Figures 3-3-3(c) and 3-3-3(f) may include fragments aligned on the graphite surface. Thus, the dissolution of a reduced TOT monoanion in the middle of the upright columnar crystals is an origin of the irreversible redox reaction of TOT. A more detailed mechanism for the deposition/dissolution and orientation changes during the redox process has not been completely understood; however, the novel microscopic

knowledge acquired using *in situ* spectroelectrochemistry can lead to a better understanding of the redox-related behaviors of stable π-radicals on graphite electrode surfaces.

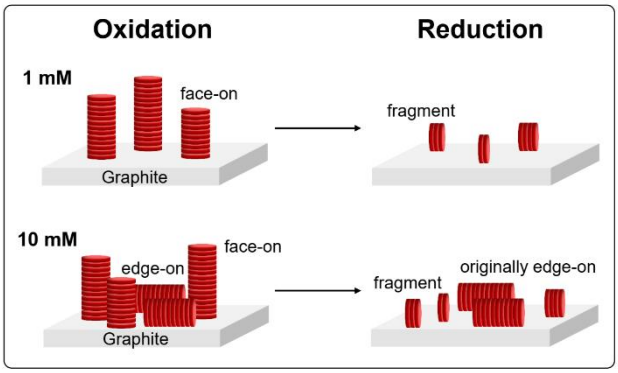

Figure 4-3-4. Schematics of the redox process and the associated structural changes of TOT on the graphite electrode surfaces.

4-4 Conclusions

In situ IR ATR spectroscopy analyses successfully confirmed that the states of the edge-on and face-on alignments of the TOT neutral radicals in the crystal were changed at different electrochemical potentials, which is consistent with the model proposed in Chapter 3. Unexpectedly, some fragments of columnar crystals were deposited on the ATR prism placed at the bottom of the IR cell during the reduction process. This indicates that the dissolution of a reduced TOT monoanion in the middle of the upright columnar crystals (face-on orientation) also occurred, in addition to the reduction of a TOT neutral radical at the top of the crystal. We believe that our study will likely lead to a better understanding of electrode design for organic active materials.

References

1. Y. Morita, S. Nishida, T. Murata, M. Moriguchi, A. Ueda, M. Satoh, K. Arifuku, K. Sato, T. Takui, *Nat. Mater.* **2011**, *10*, 947–951.
2. Y. Morita, T. Murata, A. Ueda, C. Yamada, Y. Kanzaki, D. Shiomi, K. Sato, T. Takui, *Bull. Chem. Soc. Jpn.* **2018**, *91*, 922–931.
3. H. Ito, T. Murata, T. Miyata, M. Morita, R. Tsuji, Y. Morita, *ACS Omega* **2019**, *4*, 17569–17575.
4. T. Murata, S. Nakanishi, H. Nakayama, H. Ito, M. Morita, R. Tsuji, Y. Morita, *ACS Appl. Energy Mater.* **2022**, *5*, 1218–1225.
5. D. J. Frisch, M. J.; Trucks, G. W.; Schlegel, H. B.; Scuseria, G. E.; Robb, M. A.; Cheeseman, J. R.; Scalmani, G.; Barone, V.; Mennucci, B.; Petersson, G. A.; Nakatsuji, H.; Caricato, M.; Li, X.; Hratchian, H. P.; Izmaylov, A. F.; Bloino, J.; Zheng, G.; Sonnenb, **2009**.
6. K. Kanai, T. Ikame, Y. Ouchi, K. Seki, *J. Appl. Phys.* **2009**, *105*, 023703.
7. K. Arihara, F. Kitamura, K. Nukanobu, T. Ohsaka, K. Tokuda, *J. Electroanal. Chem.* **1999**, *473*, 138–144.
8. W. Jiang, K. Yang, R. W. Vachet, B. Xing, *Langmuir* **2010**, *26*, 18071–18077.
9. J. Buijs, W. Norde, J. W. T. Lichtenbelt, *Langmuir* **1996**, *12*, 1605–1613.
10. L. Dixit, S. Ram, *Appl. Spectrosc. Rev.* **1985**, *21*, 311–418.
11. S. Garip, E. Yapici, N. S. Ozek, M. Severcan, F. Severcan, *Analyst* **2010**, *135*, 3233–3241.

Chapter 5

General Conclusions and Future Prospects

LIBs are becoming increasingly important energy storage devices as electrification progresses toward achieving targets of SDGs. Organic active materials have attracted much attention as alternatives of cathode materials for LIBs in the sense that they possess potentials to solve the problems including limitation of specific energy density, resource depletion of rare metals, and thermal runaway risk of conventional metal-oxide cathodes. TOT, a stable neutral radical with a 25π-electronic system, is a promising candidate for a practical organic cathode active material because of their high specific capacity due to four-stage redox ability and high stability due to spin-delocalized nature. In fact, superior charge/discharge properties of TOT-based cathodes have been demonstrated in bucky-paper hybrids and thin-film cathodes without any conductive additives or binders. However, cycle degradation caused by the dissolution into electrolyte solution is still a critical issue. In the TOT-based cathode system, the redox and structural behaviors during the dissolution/re-deposition upon repeating discharge/charge cycle are still unclear. The microscopic dynamics of redox behaviors should be investigated to understand the charge/discharge properties in more detail. In this dissertation, we performed voltammetry, electron microscopy and *in situ* IR spectroelectrochemistry to investigate the electrochemical dynamics of TOT on the graphite electrode surfaces.

In Chapter 3, the electrochemical behaviors and structural changes on the redox processes of TOT on the graphite electrode surface were investigated using voltammetry and electron microscopy. Voltammetry using the electrolyte solution containing TOT monoanion species indicated the irreversible redox properties between neutral radical and monoanion. SEM observation revealed the deposition and partial dissolution of TOT neutral radical crystals on the graphite electrode surface during the

oxidation and reduction, respectively. STEM analysis confirmed the crystallographic orientation of the columnar crystal. These results indicated that crystals of face-on orientation were reduced and dissolved into the electrolyte solution, whereas that of edge-on orientation were not reduced and remained on the electrode surface even at a fully reduced potential, which suggested that direct π-π interaction between a TOT molecule and graphite surface may affect the redox activity.

In Chapter 4, *in situ* IR specroelectrochemistry successfully characterized the states of face-on and edge-on orientation of TOT on the graphite electrode surface at different electrochemical potentials. The electrochemical behaviors were consistent with the model proposed in Chapter 3. Unexpectedly, it was found that some fragments of columnar crystals were deposited on the ATR prism during reduction process indicated that the dissolution of a reduced TOT monoanion in the middle of the upright columnar crystals (face-on orientation) also occurred, in addition to the reduction of a TOT neutral radical at the top of the crystal. This result suggests a possible origin of the irreversible redox reaction of TOT on the graphite electrode. As a summary, a mechanistic model on the redox process was proposed.

In conclusions, this dissertation showed that the orientations of TOT on graphite surface was important for the electron transfer characteristics. We believe that microscopic electrode design including orientation control allows to improve the performance of organic rechargeable batteries. To maintain the redox activity of TOT on graphite surfaces, the molecules should be fixed in face-on orientation even during the redox processes. Using solid electrolyte instead of electrolyte solutions may be an option for immobilizing TOT on the graphite surface because the dissolution and re-deposition should not occur in the solid electrolyte.

The following issues remained unclear and should be investigated in the future; (i) electrochemical behaviors during multi-stage redox processes, (ii) difference on the structural changes by TOT derivatives with different substituents, and (iii) electrochemical dynamics at a metallic electrode in which there is no π-π interaction such as Au (111) surface. The author hope that this dissertation will lead to a better understanding of electrode design for organic rechargeable batteries.

List of Publications

Original Paper

[1] S. Kitano, I. Tanabe, N. Shioya, T. Hasegawa, T. Murata, Y. Morita, R. Tsuji, and K. Fukui, “Voltammetric and *In Situ* Spectroscopic Investigations on the Redox Processes of Trioxotriangulene Neutral Radicals on Graphite Electrodes”, *Langmuir*, **2023**, 39, 6846-6854.

The Paper Not Included in This Dissertation

[1] Z. Bai, M. Fujii, T. Hasegawa, S. Kitano, K. Imakita, M. Mizuhata, and S. Hayashi, “Co-existence of Bi with Multiple Valence States in Zeolites - Controlling the Optical Properties by Annealing Atmosphere”, *Optical Materials*, **2011**, 34, 821–825.

[2] M. Fujii, S. Morimoto, S. Kitano, K. Imakita, J. Qiu, and H.-T. Sun, "Low-Temperature Growth of Near-Infrared Luminescent Bi-Doped SiO_xN_y Thin Films", *Optics Letters*, **2013**, 38, 4224–4227.

List of Presentations

Domestic Conferences

[1] ○北野 祥平，田邉 一郎，福井 賢一

「非水電解液／グラファイト電極界面におけるトリオキソトリアンギュレンの配向と酸化還元活性との相関」

電気化学会第 88 回大会，オンライン，2021 年 3 月（口頭発表）．

Acknowledgements

I would like to express the deepest appreciation to my supervisor, Professor Ken-ichi Fukui for providing me elaborated guidance, considerable encouragement, and invaluable discussion. I would like to express my appreciation to Associate Professor Akihito Imanishi for giving me constructive comments and warm encouragement. I would like to express my appreciation to Former Assistant Professor Ichiro Tanabe (currently Associate Professor at Rikkyo University) for his daily guidance and persistent help.

I would like to express my appreciation to Professor Yasushi Morita and Professor Tsuyoshi Murata (Aichi Institute of Technology) for providing the TOT samples and the thoughtful discussion. I would like to express my appreciation to Professor Takeshi Hasegawa and Assistant Professor Nobutaka Shioya (Kyoto University) for permission to use their laboratory equipment as well as the insightful discussion especially on IR spectroscopy. I would like to express my appreciation to Specially Appointed Professor Tadashi Itoh (Osaka University) for supporting my enrollment to the doctoral course.

I would like to express my appreciation to the members of Kaneka Corporation. I am deeply grateful to Dr. Shinji Ozawa (the director of Material Solutions New Research Engine) for permission for pursuing my doctoral dissertation as well as supporting and encouraging me throughout. I am grateful to Dr. Ryotaro Tsuji for his cooperation and useful comments. I am grateful to Dr. Yoshifumi Fukui and Dr. Yoshihisa Tawada for providing me with the opportunity to enroll in this doctoral course. I am grateful to Dr. Masamitsu Tachibana and Dr. Atsushi Tatami for providing the graphite sheet samples as well as warm encouragements. I am grateful to Dr. Ken Saito and Dr. Katsuya Fujisawa for their daily accommodating advice.

I wish to thank all the members of Fukui laboratory. Especially, I wish to thank Mr. Katsuaki Miyatani and Dr. Yusuke Morino for encouraging me as fellow working students.

Finally, I would like to extend my indebtedness to my family and parents for a lot of help and support through my daily lives.

September 2023

Shohei KITANO

(This work was financially supported by JSPS KAKENHI Grant Numbers JP22H02049, JP19H02687, and JP18H05515.)